

Systematic analysis of the nitrogen adsorption-desorption isotherms recorded for a series of microporous – mesoporous amorphous aluminosilicates using classical methods

Víctor G. Baldovino-Medrano^{a,c,d,e,*},  Viviana Niño-Celis^{b,d}, Rafael Isaacs-Giraldo^{b,*}

^a*Escuela de Ingeniería Química, Universidad Industrial de Santander, Clle 9 Cra 27, Ciudad Universitaria, Bucaramanga, (Santander) 680002*

^b*Escuela de Matemáticas, Universidad Industrial de Santander, Clle 9 Cra 27, Ciudad Universitaria, Bucaramanga, (Santander) 680002*

^c*Centro de Materiales y Nanociencias (CMN), Parque Tecnológico Guatiguará, Km. 2 vía El Refugio, Universidad Industrial de Santander, Piedecuesta (Santander), 681011, Colombia*

^d*Centro de Investigaciones en Catálisis (@CICATUIS), Parque Tecnológico Guatiguará, Km. 2 vía El Refugio, Universidad Industrial de Santander, Piedecuesta (Santander), 681011, Colombia*

^e*Laboratorio de Ciencia de Superficies (@CSSS UIS), Parque Tecnológico Guatiguará, Km. 2 vía El Refugio, Universidad Industrial de Santander, Piedecuesta (Santander), 681011, Colombia*

*Corresponding authors. E-mail: vicbaldo@uis.edu.co; rafaisaacs@saber.uis.edu.co

Abstract

Understanding the porous structure of microporous – mesoporous materials is very important for developing useful scientific concepts and principles in materials science, surface science, heterogeneous catalysis, adsorption and related technological applications. Amorphous aluminosilicates are of particular interest in this sense because it is relatively simple to design them with diverse porous structures comprising micro, meso, and even macropores. In this work, we took advantage of the latter and developed a systematic and in-depth analysis of the results of nitrogen physisorption tests at 77 K performed over a series of microporous – mesoporous amorphous aluminosilicates and of the characterization of their texture by classical models to estimate surface area and porosity. The strategy for the analysis consisted of making a thorough description of the features showed by the recorded nitrogen isotherms, first. As a result, a proposal for considering two new types of isotherms, types I(c) and IV(c), and five new types of hysteresis loops, H1(b), H2(c), H3(b), H3(c), and H4(b), in addition to the standard IUPAC classification. These new categories stemmed from the microporous – mesoporous nature of the materials and from the presence of strong network effects. The previous analysis helped interpreting and judging the results of the calculations made with classical methods to assess the texture of the materials; namely, their BET surface area, t-plot microporosity, BJH mesopore size distribution, and fractal dimension. The performed analyses allowed establishing that the relative percentage of microporosity of the materials can be correlated to the physisorption energy as described qualitatively by the C_{BET} constant. Concerning mesopore size distributions, it was found that the BJH method remains to be very valuable for describing the porous structure of the materials particularly if the results obtained with both branches of the isotherms are considered. Finally, it was shown that the fractal dimension can complement the analysis of the porous structure of microporous – mesoporous materials if the latter are compared considering the features of their isotherms and of their

hysteresis loops. Overall, the present study can thus be said to make two contributions: (i) it proposes a systematic methodology for analyzing both the raw data and the textural properties calculated by classical methods both derived from nitrogen physisorption experiments. (ii) It presents useful new insights on the texture of microporous – mesoporous materials.

Keywords: *Microporous – mesoporous materials, amorphous aluminosilicates, nitrogen physisorption isotherms, classical methods, surface area, porosity.*

1. Introduction

The physical adsorption of nitrogen (physisorption) at cryogenic temperatures (most often at 77 K; the boiling point of nitrogen) is the most used technique for characterizing the texture; i.e., surface area and porosity, of nanoporous materials. As narrated by Sing^{1,2}, the technique dates back to the beginning of the 20th century and its use for estimating the surface area of porous solids was adopted during the 1930s following the development of theoretical models by Langmuir³ and Brunauer, Emmet, and Teller⁴ for explaining the adsorption of gases and vapors over solids. Further advances during the late 1940s⁵ and early 1950s⁶ led to the development of methods that apply the Kelvin equation for estimating the pore size distribution of solids where capillary condensation occurs during the nitrogen physisorption tests. This type of pores were later named mesopores and their size ranges between 2.0 and 50.0 nm.⁷ Further studies by Dubinin and his group⁸ established the basis for studying pores smaller than 2.0 nm. All the above efforts and many other more^{9–14} provided researchers with a relatively complete set of tools (classical models) to analyze physisorption isotherms in order to estimate the surface area and porosity of materials. Furthermore, the very rapid development of molecular level calculations by the density functional theory during the 1990s has led to more modern models for assessing texture in nanoporous materials.^{15,16} However, the access and number of the latter models is still very limited because of the complex calculations that need to be carried out and because their accuracy strongly depends on the particular chemistry of each type of adsorbent. Consequently, classic models^{1,17–22} are still the most used in the field because their usefulness triumphs their strong shortcomings. Proof of this is that all modern equipment comes provided with automated software that allows to comfortably do estimations of surface area and porosity with classic models with a couple of clicks.

However, comfortability in science often comes at the expense of critical thinking. Nowadays, scores of scientific reports routinely report nitrogen physisorption data and the textural properties thereafter derived without an in-depth analysis of the recorded data or criticism of the results obtained after applying the models for assessing texture. Furthermore, there is an unhealthy trend to omit the experimental details of the test, even though clear recommendations have been published in several books,^{11,23–26} reviews,^{27–30} IUPAC reports,^{7,31} and some in international standards.³²

In this contribution, a critical assessment of the nitrogen adsorption-desorption isotherms of a series of materials based on amorphous silica-aluminas and of the data thereof derived to characterize their texture is done. Namely, a set of amorphous silica-aluminas were tested in nitrogen physisorption experiments before and after loading them with nickel and molybdenum oxide by wet impregnation.^{33,34} These materials are normally applied for hydroprocessing reactions.^{35–37} The paper fulfills two purposes. First, providing practical guidance on how to qualitatively analyze the data measured during nitrogen physisorption

tests; i.e., the recorded isotherms and on how to put this data in the service of interpreting and judging the results of the calculations of surface area and porosity made via classic methods. Second, it is demonstrated that the above method of analysis fruitfully leads to better interpretation and advances in the knowledge of the structure of nanoporous materials. The strategies for analysis presented in the paper seem particularly handy when dealing with materials that exhibit both micropores and mesopores; a type of materials often found in many scientific and industrial applications.^{19,35,36,38–48}

2. Experimental and analytical methods

2.1 Analyzed materials. The analyzed amorphous silica-aluminas were synthesized by three variations of the sol-gel method; namely, sol-gel via hydrolysis in acidic medium (ASA),⁴² a sol-gel method where polyethylene glycol (ASAP)⁴³ was used as a template, and another where a so-called gel skeletal reinforcing solution (ASAR) composed of tetraethylorthosilicate (TEOS) and 2-propanol was employed for the synthesis. Further impregnation of a Ni-MoO_x phase was made to these amorphous silica-aluminas (NiMo) whose primary application was the refining of heavy crude oil cuts.^{44,45} Specific details for the synthesis of the materials are reported by Coconubo³⁶ and Duarte.³⁵ For the purposes of the current work, the materials were branded as ASA###, ASAP##, ASAR###, and NiMo/ASA###, NiMo/ASAP##, and NiMo/ASAR###. Where, # was an internal code assigned to each material. A total of 34 materials; 17 amorphous silica-aluminas and their 17 impregnated amorphous silica-aluminas counterparts were analyzed in the present study.

2.2 Nitrogen physisorption measurements. Nitrogen physisorption isotherms were recorded at 77 K with a 3Flex instrument from Micromeritics. Prior to measurements, samples of the materials whose weight was between ca. 0.1000 and 0.2000 g were put in an outgassing unit operated under vacuum (~0.05 mbar) at 573 K for one night. Equilibrium adsorption isotherms were recorded within a relative pressure, P/P₀, range between ~2.0×10⁻³ and ~0.998 using 10 s equilibration intervals.

2.3 Assessment of porosity, surface area, and fractal dimension. The nature and characteristics of the porous network of the materials was qualitatively assessed from the shape of the recorded isotherms and from the shape of the corresponding hysteresis loops considering IUPAC recommendations^{31,49} and other literature works.^{19,29,30,49–53} Afterwards, the surface area of the materials was assessed by the Brunauer-Emmet-Teller (BET) method⁴ applying the so-called Rouquerol consistency criteria.¹⁷ The contribution of microporosity to the surface area of the materials was assessed with the t-plot method⁵⁴ and applying the Harkins and Jura reference isotherm.^{9,10} This method proved to produce the most satisfactory results for fitting the recorded isotherms. Calculations for assessing the micropore size distribution of the materials were not made because of the restricted lower P/P₀ limit used during the physisorption tests. On the other hand, mesopore size distributions were estimated with the Barret-Joyner-Halenda (BJH) method⁶ using the Harkins and Jura standard isotherm¹⁰ with the Faas correction. The latter employs the concept of thickness of an adsorbed layer in a circular pore versus the simple application of thickness on a flat surface. All of the above calculations were done with the *MicroActive*® software provided with the 3Flex apparatus.

Finally, the fractal dimension of the materials was estimated in an attempt to analyze the complexity of their porous network.⁵⁵ Four methods were tested for this purpose; the Pfeifer et al.^{56,57} adaptation of the Frenkel-Halsey-Hill method, the thermodynamic method proposed by Neimark,^{55,58} the Wang and Li method,⁵⁹ and the Sandoval et al. method.⁶⁰ Among these four, only the results obtained with the method by Sandoval et al.⁶⁰ will be presented in the paper since the other three either sometimes produced values of the fractal dimension without physical sense; namely, fractal dimensions larger than 3 or did not showed an adequate linear fit of the data (see Supporting Information, **Figure S3** and **Table S1**). All these calculations were made by setting-up an Excel workbook where conventional numerical methods were used for fitting the data.⁶¹

3. Results and discussion

3.1 Characteristics of the adsorption isotherms

3.1.1 Classification of the isotherms. **Figures 1** and **2** represent the different types of N₂ physisorption isotherms recorded for the studied materials while **Table 1** describes the characteristics of all the isotherms recorded for this work. The full set of isotherms are shown in **Figure S1** of the Supplementary Information. To explain the notes presented in Table 1, it is important to recall the classification of isotherms made by IUPAC in its most recent technical report.³¹ For the sake of brevity, we will refer only to the isotherms akin to those found in the present work; namely, types I and II, and subtype IV(a). We apologize with the expert reader who is already well acquainted with this information.

Table 1. Characteristics of the N₂ physisorption isotherms recorded for the studied materials.

Materials	Isotherm type*	Hysteresis loop
ASAP26, ASAP28, ASAP36, ASAP38, ASAP48, NiMo/ASAP28, NiMo/ASAP36, NiMo/ASAP26,	Combination of IUPAC types I(b), II, and IV(a). Proposed classification: Type I(c).	Variation of IUPAC type H4 with inverted wedge shape. The loop closes at P/P ₀ ~ 0.41 after a steep drop of the desorption branch of the isotherm at P/P ₀ ~ 0.49. Proposed classification: H4(b).
ASAP18, NiMo/ASAP38, NiMo/ASAP18, NiMo/ASAP48,		Variation of IUPAC type H4 with lanceolate half leaf shape. The loop closes at P/P ₀ ~ 0.42 after a steep drop of the desorption branch of the isotherm at P/P ₀ ~ 0.49. Proposed classification: H4(a).
ASA095, NiMo/ASA050	IUPAC type IV(a): Inflection point at P/P ₀ ~ 0.79 or at P/P ₀ ~ 0.91 – 0.96 followed either by a slightly inclined plateau or by a plateau.	Mixture of IUPAC H2(a) and H3: Loops have inclined mound shape. They close around P/P ₀ ~ 0.41 after steep drop of the desorption branch at P/P ₀ ~ 0.52, and the adsorption and desorption branches separate at P/P ₀ ~ 0.79 with wide gaps. Proposed classification: H2(c).
ASAR568, ASAR586, ASAR588, NiMo/ASAR568,		Mixture of IUPAC types H1 and H3 with bean pod shape showing inflection point at P/P ₀ ~ 0.73 and closure at P/P ₀ ~ 0.50. Proposed classification: H1(b).

NiMo/ASAR586, NiMo/ASAR588		
ASAR085, NiMo/ASAR085		Similar to IUPAC type H1 with inverted horn shape and closure at $P/P_0 \sim 0.63$. Proposed classification: H1(a).
ASA050, ASA075, ASA085, NiMo/ASA075, NiMo/ASA085,	Semi IUPAC type IV(a): (very steep) unrestricted adsorption and hysteresis with some (the latter two in the previous column) showing two inflection points. Proposed classification: Type IV(c).	Variation of IUPAC type H3 with empanada shape showing inflection point at $P/P_0 \sim 0.87$ and closure at $P/P_0 \sim 0.46$. Proposed classification: H3(b).
ASAR065, ASAR075, ASAR566, NiMo/ASAR075, NiMo/ASAR566		IUPAC type H3 with very narrow gap between the adsorption and desorption branches of the isotherm. The loop closes at $P/P_0 \sim 0.56$. Proposed classification: H3(a).
NiMo/ASA095, NiMo/ASAR065		Variation of IUPAC type H3 with empanada shape showing inflection point at $P/P_0 \sim 0.82$ followed by inverted semi-horn shape. The loop closes at $P/P_0 \sim 0.43$. Proposed classification: H3(c).

IUPAC's type I isotherms are exhibited by solids constituted by micropores. These isotherms are completely reversible; i.e., they do not show hysteresis, they are concave to the relative pressure axis, and, after micropore filling,⁸ the amount of adsorbate reaches a limiting value up to the highest P/P_0 value measured during the experiment. There are two subtypes of the type I isotherm. Subtype I(a) exhibits a very steep initial increase in the amount of adsorbed N_2 at the P/P_0 range defined for micropore filling; which is between 0.005 and ~ 0.050 according to Bardestani et al.²⁹ Such a phenomenon is attributed to the strong interaction between the adsorbate and the walls of pores whose width is ca. 1.0 nm.³¹ When the width of the micropores is larger than the aforementioned value and up to ca. 2.5 nm, the initial increase in the amount of adsorbed N_2 is lower and a more pronounced change in curvature is found hence producing the subtype I(b) isotherm in IUPAC's system.³¹ However, in general, IUPAC³¹ has not defined a typical range for the amount of nitrogen that is adsorbed by microporous materials.

IUPAC's type II isotherms are also completely reversible and have an S-shape; i.e., they are concave to the P/P_0 axis in the low relative pressure region followed by a semi-linear section, and, finally, they become convex to the axis at the high relative pressure region of the isotherm. Near $P/P_0 = 1.0$, the amount of adsorbed N_2 can increase "without limit" according to IUPAC.³¹ The S-shape of the isotherm behavior is attributed to unrestricted monolayer-multilayer adsorption after the initial completion of the theoretical/statistical monolayer⁴ of adsorbate but the unlimited adsorption of N_2 near $P/P_0 = 1.0$ is not explained in IUPAC's report.³¹ Typically, nonporous and macroporous (i.e., materials whose pores are larger than 50 nm³¹) show IUPAC's type II isotherms but the S-shape of this isotherm is basically the same as that of IUPAC's type IV isotherms.

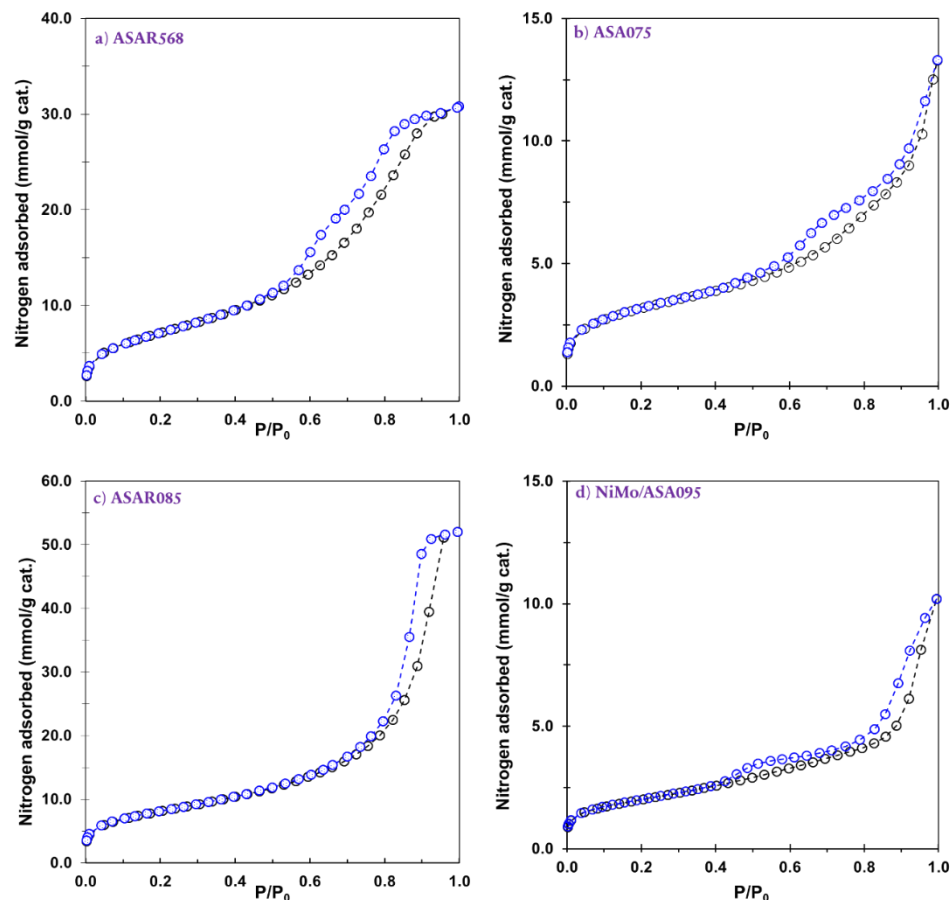


Figure 1. First group of four representative N_2 sorption isotherms (77K) for the studied materials. a) ASAR568: Semi (IUPAC³¹) type IV(a) isotherm with hysteresis showing a bean pod shape; b) ASA075: Semi (IUPAC³¹) type II isotherm with empanada shape hysteresis; c) ASAR085: Semi (IUPAC³¹) type IV(a) isotherm with hysteresis showing a vertically oriented inverted horn shape; and, d) NiMo/ASA095: Semi (IUPAC³¹) type II isotherm with hysteresis having a combination of empanada and inclined inverted cone shapes.

Finally, the shape of IUPAC's subtype IV(a) isotherms is similar to that of type II, but they show irreversibility as manifested by their distinct hysteresis loops in the relative pressure region after $P/P_0 \sim 0.4$. For tests made with N_2 at 77 K, it is said that hysteresis is produced by capillary condensation in mesopores whose width is wider than ca. 4.0 nm.³¹ After hysteresis, type IV(a) isotherms normally show a saturation plateau of variable length; including some cases where a mere inflection point is found.³¹

Considering the above, **Table 1** summarizes the classification made for the recorded isotherms. They were classified in three types; namely, type I(c) for 12 out of the 34 materials, type IV(a) for 10 out of the 34 materials, and type IV(c) for 12 out of the 34 materials. Among the latter, types I(c) and IV(c) are categories proposed in this work. The proposed type I(c) isotherm is a combination of IUPAC's types I(b), II, and IV(a) isotherms which indicates that the material has both micropores and mesopores. It is somehow surprising that the literature has not made a formal proposal for classifying these isotherms apart even though classic papers such as the one by Shull et al.⁵ already presented cases such as the ones found in this work. In addition, Schneider⁵² admitted that "adsorption isotherms of real porous material represent usually a combination of these [IUPAC standard] types".

Furthermore, the recent update of IUPAC's technical report on the physisorption of gases³¹ only considered fully reversible isotherms for microporous materials hence excluding a particular category for microporous-mesoporous materials showing irreversibility due to capillary condensation-evaporation phenomena in mesopores. The latter, despite the humongous number of materials that follow into this category such as some amorphous silica-aluminas,⁵ molecular organic frameworks^{46,47,62,63}, and zeolites both classic such as ZSM-5^{64,65} and hierarchical ones.^{39,40}

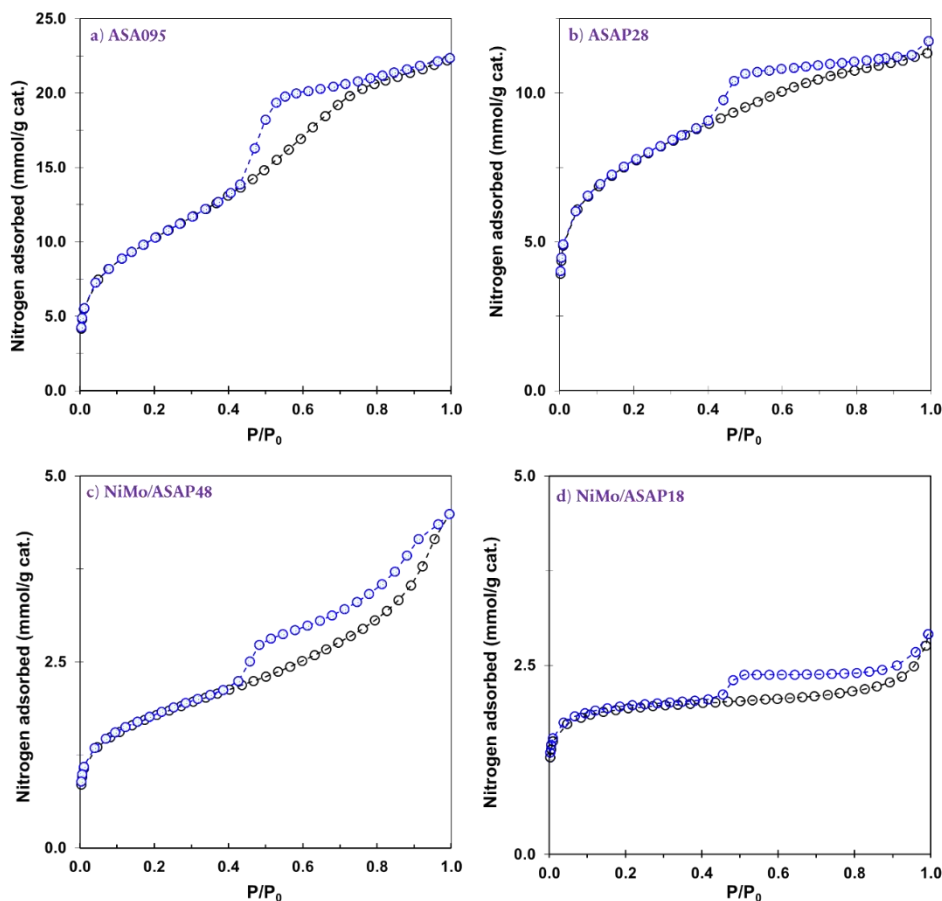


Figure 2. Second group of four representative N_2 sorption isotherms (77K) for the studied materials. a) ASA095: Semi (IUPAC³¹) type IV(a) isotherm with inclined mound shape hysteresis; b) ASAP28: Semi (IUPAC³¹) type II isotherm with inverted wedge shape hysteresis; c) NiMo/ASAP48: Semi (IUPAC³¹) type II isotherm with inclined lanceolate half leaf shape hysteresis; and, d) NiMo/ASAP18: Semi (IUPAC³¹) II isotherm with horizontal and inverted horn shape hysteresis.

The other proposed category is type IV(c). In this instance, though the isotherm could be classified as a type IV(a), the fact that it displays unlimited adsorption at $P/P_0 > 0.7$ makes it inadequate to classify it as such, in our opinion. Furthermore, type IV(c) isotherms found herein may also show multiple inflection points instead of the plateau that is characteristic of IUPAC's type IV isotherms. Isotherms with unlimited adsorption are normally associated with unfilled macropores³¹ or with materials formed by non-rigid aggregates of platy particles.⁶⁶ So far, IUPAC does not consider this feature of the isotherm within its classification for the type of isotherm but rather as a feature of the so-called H3 hysteresis loop (more on this below). The association of this behavior to the platy nature of the particles

of the porous solid agrees with what is known for mesoporous oxides such as γ -Al₂O₃⁶⁷ and parent aluminum containing mixed oxides.^{68,69} Multiple inflection points at $P/P_0 > 0.7$ are also commonly observed when the accumulation of extraneous materials over mesopore mouths takes place; e.g., carbonaceous residua over fluid catalytic cracking catalysts.⁶⁸ Herein, the catalysts NiMo/ASA095 and NiMo/ASAR065 were the ones that displayed such type of behavior. Therefore, it is reasonable to assume that the impregnated metals accumulated either on the mouths or inside the mesopores of the corresponding amorphous aluminosilicates.

3.1.2 Hysteresis loops. Concerning the hysteresis loops found for the studied materials, **Table 1**, two materials were considered to have IUPAC's H1 loop, six showed a mixture of IUPAC types H1 and H3, two showed a mixture of H2(a) and H4 loops, five showed IUPAC type H3 loops, twelve showed a variation of the H3 loop, and another twelve showed a variation of the H4 loop. Therefore, all except the IUPAC type H5 hysteresis loop³¹ were identified in the tested materials. Several of the recorded loops were either variations (strong variations in some cases -**Figures 1, 2, and S1**) or mixtures of the IUPAC's loops. Consequently, we propose five new categories for hysteresis loops; namely, H1(b), H2(c), H3(b), H3(c), and H4(b), while the standard H1, H3, and H4 IUPAC loops may now be called H1(a), H3(a), and H4(a) loops, respectively.

3.1.2 Hysteresis loops. Concerning the hysteresis loops found for the studied materials, **Table 1**, two materials were considered to have IUPAC's H1 loop, six showed a mixture of IUPAC types H1 and H3, two showed a mixture of H2(a) and H4 loops, five showed IUPAC type H3 loops, twelve showed a variation of the H3 loop, and another twelve showed a variation of the H4 loop. Therefore, all except the IUPAC type H5 hysteresis loop³¹ were identified in the tested materials. Several of the recorded loops were either variations (strong variations in some cases -**Figures 1, 2, and S1**) or mixtures of the IUPAC's loops. Consequently, we propose five new categories for hysteresis loops; namely, H1(b), H2(c), H3(b), H3(c), and H4(b), while the standard H1, H3, and H4 IUPAC loops may now be called H1(a), H3(a), and H4(a) loops, respectively.

The proposed type H1(b) is a mixture of IUPAC's H1 and H3 types making a bean pod shape with an intermediate inflection point between $P/P_0 \sim 0.50 - 0.75$, **Figures 1a) and S1h) - S1i)**. IUPAC^{31,70} assigns H1 hysteresis to loops whose raise in the amount of physisorbed nitrogen is steep and that are given by well-ordered mesopore networks with pore shapes that may either be tubular or ink-bottle. For the latter, the neck width is near the same as the pore cavity. Meanwhile, IUPAC characterizes H3 loops as those produced either by non-rigid platy particles or by a pore network comprising macropores which are not filled by condensed nitrogen during the measurement.

The proposed H2(c) loop was a mixture of IUPAC's type H2(a) and H3 whose shape resembled an inclined mound, **Figures 2a) and S1f)**. According to IUPAC,³¹ H2(a) loops are produced when either the pore network has necks that may induce cavitation or pore blocking/percolation during desorption since such phenomena may cause a characteristic steep drop in the amount of nitrogen desorbed from the sample during the test. Considering the combination of the aforementioned features of H2(a) and H3 loops, it seems more

adequate to add a new category, H2(c), for the loops found for the materials featured in Figures **2a)** and **S1f)**.

Both the proposed H3(b) and H3(c) loops distinguished themselves by displaying an empanada like shape before the closure of the hysteresis loop, Figures **1b)**, **1d)**, and **S1a) - S1e)**. The differences between H3(b) and H3(c) were the location of the inflection point after the empanada feature of the loop and a longer semi-linear section for the adsorption branch of the materials showing the latter loop, compare Figures **1d)** and **S1a)** with Figures **1b)** and **S1b) – S1f)**, respectively.

Finally, the proposal of the H4(b) loop responds to the fact that IUPAC H4 loops are represented with an adsorption branch that reaches a very extended plateau after micropore filling.³¹ Conversely, the materials that showed the H4(b) loop, Figures **2b)** and **S1r) – S1w)** had very pronounced downward concavity in regards to the P/P_0 axis without ever reaching a plateau during the measurements.

3.2 Characterization of texture from calculations made with classic models

3.2.1 Surface area and type of porosity. Table 2 shows the values of the BET surface area (S_{BET}), C_{BET} parameter, microporous surface area (Micro-SA), the so-called external, -i.e., mesoporous plus macroporous- surface area, (Exter-SA), the percentage of microporous surface area ($\xi = \% \text{Micro-SA}$), the types of isotherm and hysteresis loop, as in agreement with the classification discussed above and summarized in **Table 1**, and a classification of the porosity of the materials. The latter was done according to the following criteria: if $\xi \leq 10\%$, the material was classified as mesoporous, if $10\% < \xi \leq 40\%$, the material was classified as microporous-mesoporous with mesoporosity being prevalent, if $40\% < \xi \leq 60\%$, the material was classified as microporous-mesoporous, if $60\% < \xi \leq 90\%$, the material was classified as microporous-mesoporous with microporosity being dominant, and, if $\xi \geq 90\%$ the material was classified as microporous.

According to the collected data, the following observations were made: (i) ~44.1% of the materials were mesoporous; ~32.4% of the materials were microporous-mesoporous with the mesoporosity being prevalent; ~11.8% of the materials were microporous-mesoporous with no dominant type of porosity; the same percentage of materials as above were microporous-mesoporous with microporosity being prevalent; and, finally, the remaining (1/34) ~2.9% of the materials were microporous. (ii) The classification for the type of isotherm proposed in **Table 1** was coherent with the classification of porosity made in **Table 2**. Therefore, the materials whose isotherms were classified either as IV(a) or IV(c) showed a prevalence of mesoporosity. Meanwhile, the materials whose isotherms were classified as I(c) showed well developed microporosity; namely, they were microporous or microporous-mesoporous materials where either no prevalent type of porosity was found or microporosity was dominant.

Table 2. Surface area calculations; total (S_{ABET}), microporous (Micro-SA), and external (Exter-SA) for the studied materials. All surface areas are expressed in m^2/g . *Values estimated using the t-plot method with the Harkins and Jura standard isotherm.⁵⁴ **Calculated as: $\xi = 100 \times (\text{Micro-SA} / (\text{Micro-SA} + \text{Exter-SA}))$. ***As in agreement with the classification proposed in Table 1. ****Meso = mostly mesoporous ($\xi \leq 10$), micro-MESO = microporous-mesoporous material where mesoporosity is dominant ($10 < \xi \leq 40$), micro-meso = microporous-mesoporous material ($40 < \xi \leq 60$), MICRO-Meso = microporous – mesoporous material where microporosity is dominant ($60 < \xi \leq 90$), and Micro = mostly microporous material ($\xi > 90$).

Material code	S_{ABET}	C_{BET}	Micro-SA*	Exter-SA*	$\xi = \% \text{Micro-SA}^{**}$	Isotherm***	Hysteresis***	Porosity****
ASA050	342.5	80	0.6	341.9	4.9	IV(c)	H3(b)	Meso
NiMo/ASA050	72.1	110	6.0	66.1	9.0	IV(a)	H2(c)	Meso
ASA075	261.6	97	35.6	226.0	29.7	IV(c)	H3(b)	micro-MESO
NiMo/ASA075	68.7	171	15.9	52.7	26.2	IV(c)	H3(b)	micro-MESO
ASA085	477.2	104	75.3	401.9	19.4	IV(c)	H3(b)	micro-MESO
NiMo/ASA085	133.1	127	20.3	112.8	17.8	IV(c)	H3(b)	micro-MESO
ASA095	838.3	86	60.8	777.5	8.2	IV(a)	H2(c)	Meso
NiMo/ASA095	162.8	106	15.8	147.0	9.2	IV(c)	H3(c)	Meso
ASAP18	407.0	722	302.5	104.5	84.7	I(c)	H4(a)	MICRO-Meso
NiMo/ASAP18	163.6	984	123.7	39.9	90.3	I(c)	H4(a)	Micro
ASAP26	577.5	544	361.8	215.7	75.3	I(c)	H4(b)	MICRO-Meso
NiMo/ASAP26	320.2	357	178.0	142.2	76.6	I(c)	H4(b)	MICRO-Meso
ASAP28	630.2	171	218.6	411.6	48.8	I(c)	H4(a)	micro-meso
NiMo/ASAP28	392.4	171	120.0	272.5	40.9	I(c)	H4(b)	micro-meso
ASAP36	638.5	290	349.8	288.7	63.5	I(c)	H4(b)	MICRO-Meso
NiMo/ASAP36	458.8	230	203.9	254.9	56.7	I(c)	H4(b)	micro-meso
ASAP38	656.7	206	281.2	375.4	26.2	I(c)	H4(b)	micro-MESO
NiMo/ASAP38	222.5	226	101.9	120.6	57.7	I(c)	H4(a)	micro-meso
ASAP48	692.2	96	98.9	593.3	23.7	I(c)	H4(b)	micro-MESO
NiMo/ASAP48	144.1	138	32.3	111.8	33.0	I(c)	H4(a)	micro-MESO
ASAR065	584.5	90	12.5	572.0	2.4	IV(c)	H3(a)	Meso
NiMo/ASAR065	289.4	81	0.0	289.7	0.8	IV(c)	H3(c)	Meso
ASAR075	605.8	95	48.2	557.5	8.0	IV(c)	H3(a)	Meso

NiMo/ASAR075	224.9	133	29.6	195.3	17.2	IV(c)	H3(a)	micro-MESO
ASAR085	656.4	103	57.2	599.2	8.9	IV(a)	H1(a)	Meso
NiMo/ASAR085	333.3	108	42.1	291.2	17.4	IV(a)	H1(a)	micro-MESO
ASAR566	522.9	89	20.0	502.9	5.2	IV(c)	H3(a)	Meso
NiMo/ASAR566	188.6	130	25.0	163.6	19.0	IV(c)	H3(a)	micro-MESO
ASAR568	495.3	81	0.0	498.5	0.0	IV(a)	H1(b)	Meso
NiMo/ASAR568	354.3	82	17.4	336.9	5.9	IV(a)	H1(b)	Meso
ASAR586	503.8	75	0.0	514.5	0.0	IV(a)	H1(b)	Meso
NiMo/ASAR586	314.2	119	35.4	278.8	14.6	IV(a)	H1(b)	micro-MESO
ASAR588	465.9	74	0.0	485.2	0.0	IV(a)	H1(b)	Meso
NiMo/ASAR588	309.8	96	28.8	281.0	11.6	IV(a)	H1(b)	micro-MESO

Besides the above, it was interesting to analyze the correlation between the micropore surface area of the materials and the so-called C_{BET} constant. In this sense, trying to directly correlate these two parameters proved fruitless, **Figure S2**. Conversely, a correlation between the percentage of microporosity and C_{BET} was found, **Figure 3**. The found correlation suggests an exponential dependency of C_{BET} with ξ , as follows: $C_{BET} = a + \frac{b}{1 + (\frac{\xi}{c})^d}$. This

correlation is mathematically complex since it is an exponential function that includes four parameters. However, it can be pointed out that this type of equations are rather characteristic of transport processes.⁷¹ In general, one may consider that the correlation between C_{BET} and ξ is composed of a semi-linear part and of an exponential part, **Figure 3**, with the former comprising data up to $\xi \approx 20\%$, where the C_{BET} values were between 74 and 133.

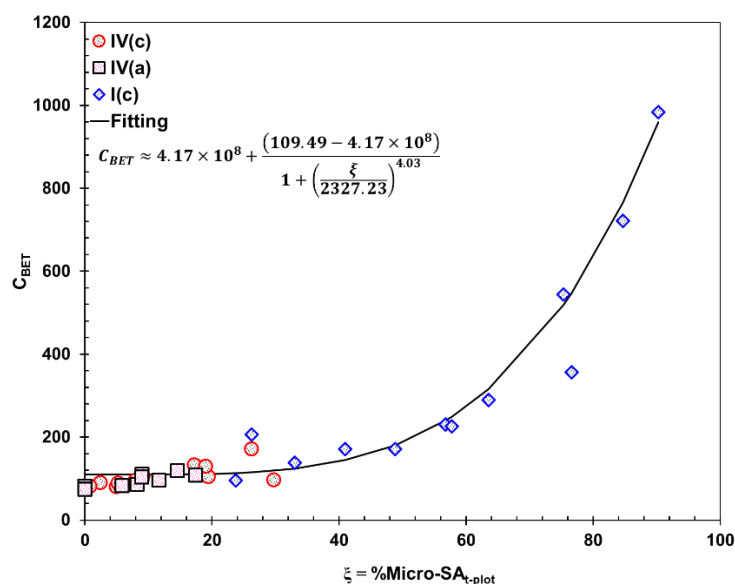


Figure 3. Correlation between C_{BET} and the percentage of microporosity (ξ) of the studied set of materials as distinguished by the type of physisorption isotherm. Fitting made via: <https://mycurvefit.com/>.

Considering the definition for C_{BET} : $C_{BET} = e^{\frac{(E_1 - E_L)}{RT}}$,⁴ where, E_1 is the heat of adsorption of the first statistical layer of adsorbate, E_L is the heat of liquefaction of the adsorbate, R the universal gas constant ($\approx 1.9872 \text{ cal} \times \text{K}^{-1} \times \text{mol}^{-1}$), and T is the temperature of the physisorption test (77 K, herein), one may assess how the BET apparent energy of adsorption ($\Delta E_{\text{ads}}^{\text{App}} = (E_1 - E_L)$) was statistically distributed for the studied samples. To do this, we made an Averaged Shifted Histogram⁷² of the data using the app available in the website: <https://maverick.chem.ualberta.ca/plot/ash>, **Figure 4**. Accordingly, as a random variable, $\Delta E_{\text{ads}}^{\text{App}}$ was better described by a platykurtic (i.e., short-tailed -kurtosis < 3 -) distribution with positive skewness (~ 1.56). Hence, considering the information presented in **Figures 3** and **4**, one may assume that the higher the percentage of microporosity of the materials, the stronger the interaction between the adsorbate and the adsorbent was. Furthermore, as earlier mentioned, the relationship between these parameters seems to be related to transport processes.

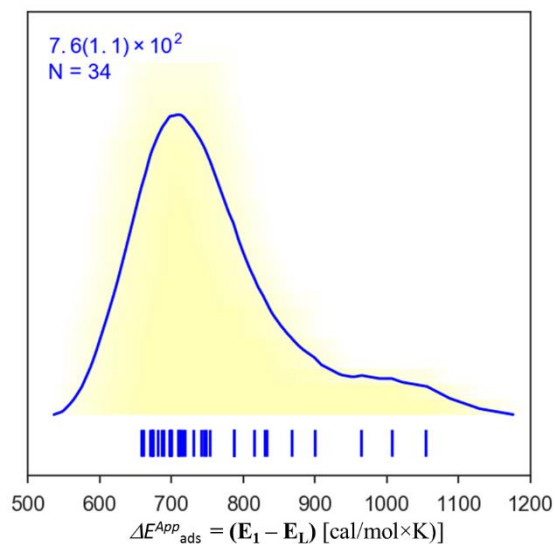


Figure 4. Average Shifted Histogram for the distribution of the BET apparent adsorption energies of the tested materials. Plot made with the app provided by: <https://maverick.chem.ualberta.ca/plot/ash>.

3.2.2 Characterization of porosity. Transport processes depend strongly on pore size distributions, of course.⁷³ Herein, porosity was assessed only for the mesoporous range since data for $P/P_0 < 1 \times 10^{-3}$ was not available. As announced in the Experimental section, the analysis of mesoporosity was done with the BJH method⁶ using the Harkins and Jura standard isotherm¹⁰ with the Faas correction. For the analysis, both the adsorption and the desorption branches of the isotherms were considered for performing the calculation of the pore size distributions, **Figures 5 to 12**. These figures included not only the produced pore size distributions but also a zoom of the region of the corresponding isotherms where the hysteresis loops closed. The latter was used to analyze the probable influence of the so-called tensile strength effect^{22,74} on the distributions estimated from the desorption branch of the isotherm. Considering the number of materials that were tested and the classification of their isotherms and hysteresis loops, **Tables 1 and 2**, it was more practical to tabulate the observations made on the estimated pore size distributions from each branch of the adsorption isotherm for the families of materials that showed the same kind of isotherms and hysteresis loops, **Tables 3 to 8**.

In general, all pore size distributions from the type I(c) isotherms, **Figures 5 and 6**, and those from the IV(a) type of isotherm with H2(c) hysteresis, **Figure 9**, showed a peak due to the tensile strength effect at 3.68 ± 0.04 nm (t-Student 95% confidence interval with 13 degrees of freedom) in the pore size distributions derived from the desorption branch of the isotherms, **Figures 5 and 6**. The latter value is very similar to the 3.8 nm value reported by Groen et al.²² The tensile strength effect is associated to a sudden closure of the hysteresis loop between $0.41 \leq P/P_0 \leq 0.48$.²² It arises when the network of mesopores has a stochastic nature and it is to some extent interconnected which causes the so-called network effects leading to cavitation during the desorption of the nitrogen adsorptive.²² In practice, as seen in **Figures 5 and 6**, this often generates a tall and sharp peak in the distribution estimated from the desorption branch of the isotherm. The artifact then consists on considering that this peak is indicative of the fact that the mesoporosity of the material is dominated by a family

of pores whose pore size is very narrow; a fact that is not corroborated by the distribution of pore sizes derived from the adsorption branch of the isotherm. A contrast between the two pore size distributions rather indicates that the network of mesopores includes pores of the size associated to the tensile strength effect but these pores are not particularly remarkable within the pore size distribution. Instead, as evidenced by the results featured in **Figures 5** and **6**, the distribution of sizes for the mesoporous network of the examined microporous – mesoporous materials may span the whole range of mesoporosity. On the other hand, regardless of the branch of the isotherm considered for the calculations, the curves for pore size distribution for the materials with the type I(c) isotherm were characterized by a monotonic decrease which is a mathematic consequence of the fact that the rate of change of the amount of adsorbed nitrogen constantly decreased as a function of the width of the pores.

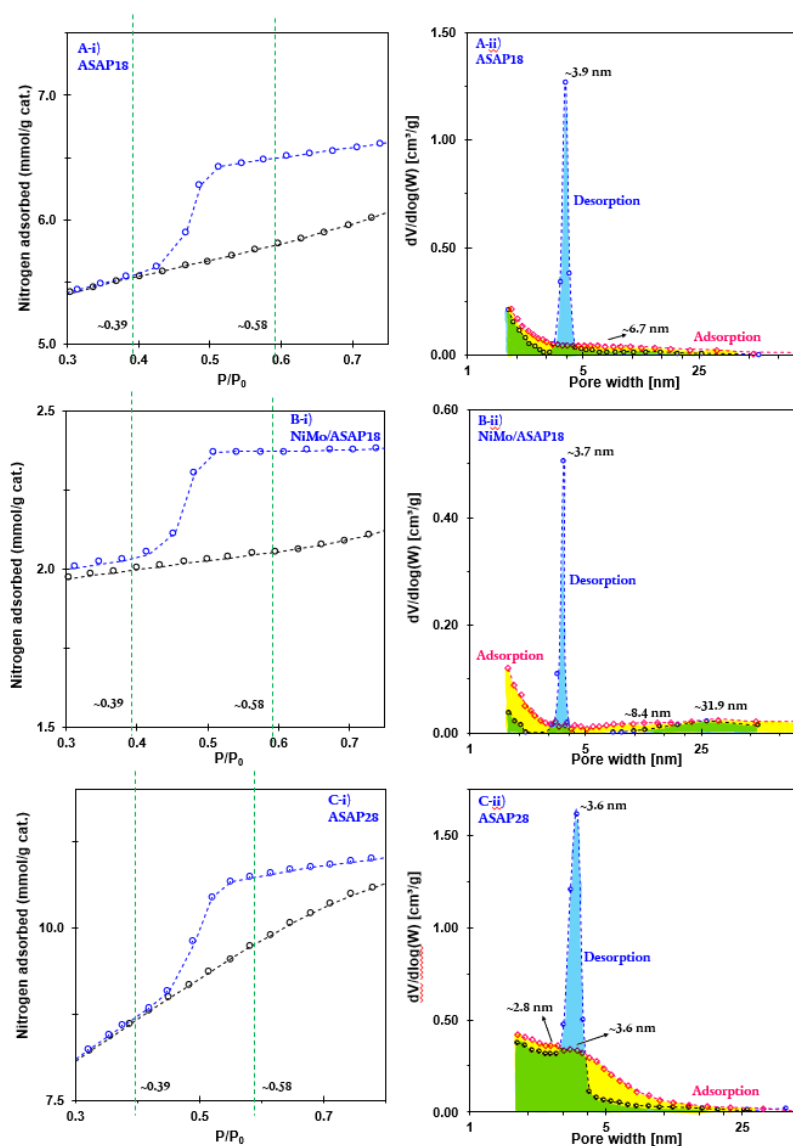


Figure 5. Details of the closure of the hysteresis loops for selected samples exhibiting I(c) isotherms with H4(a) hysteresis loop and pore size distributions as estimated from both the adsorption and the desorption branches of the isotherms by using the BJH method⁶ with the Harkins and Jura standard isotherm¹⁰ and the Faas correction.

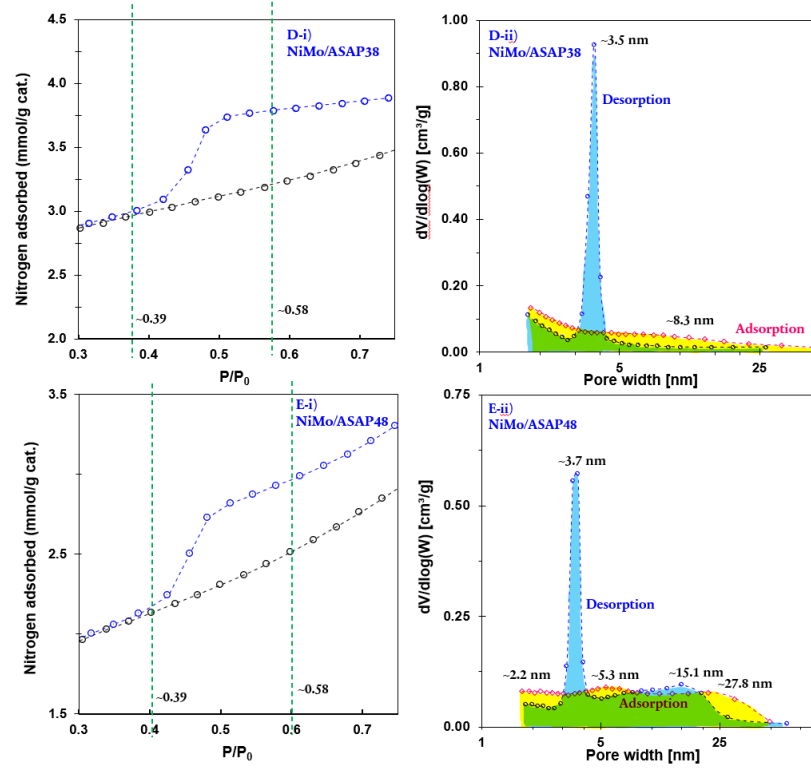


Figure 5. Continuation.

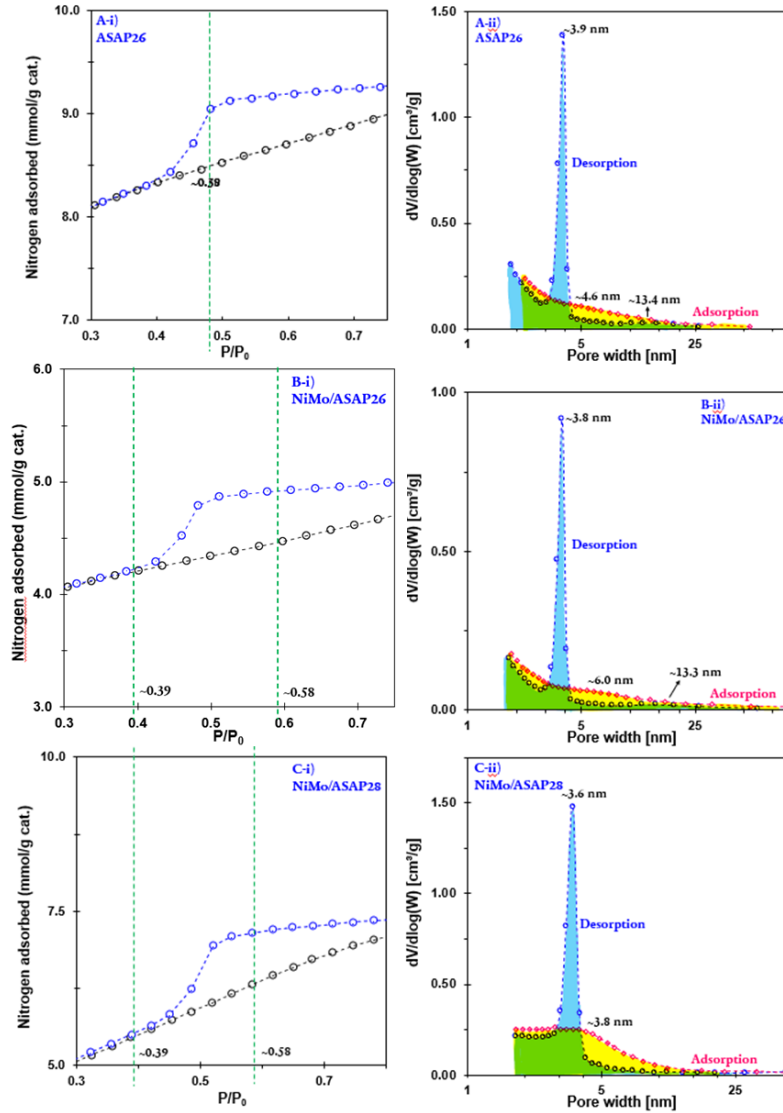


Figure 6. Details of the closure of the hysteresis loops for selected samples exhibiting I(c) isotherms with H4(b) hysteresis loop and pore size distributions as estimated from both the adsorption and the desorption branches of the isotherms by using the BJH method⁶ with the Harkins and Jura standard isotherm¹⁰ and the Faas correction.

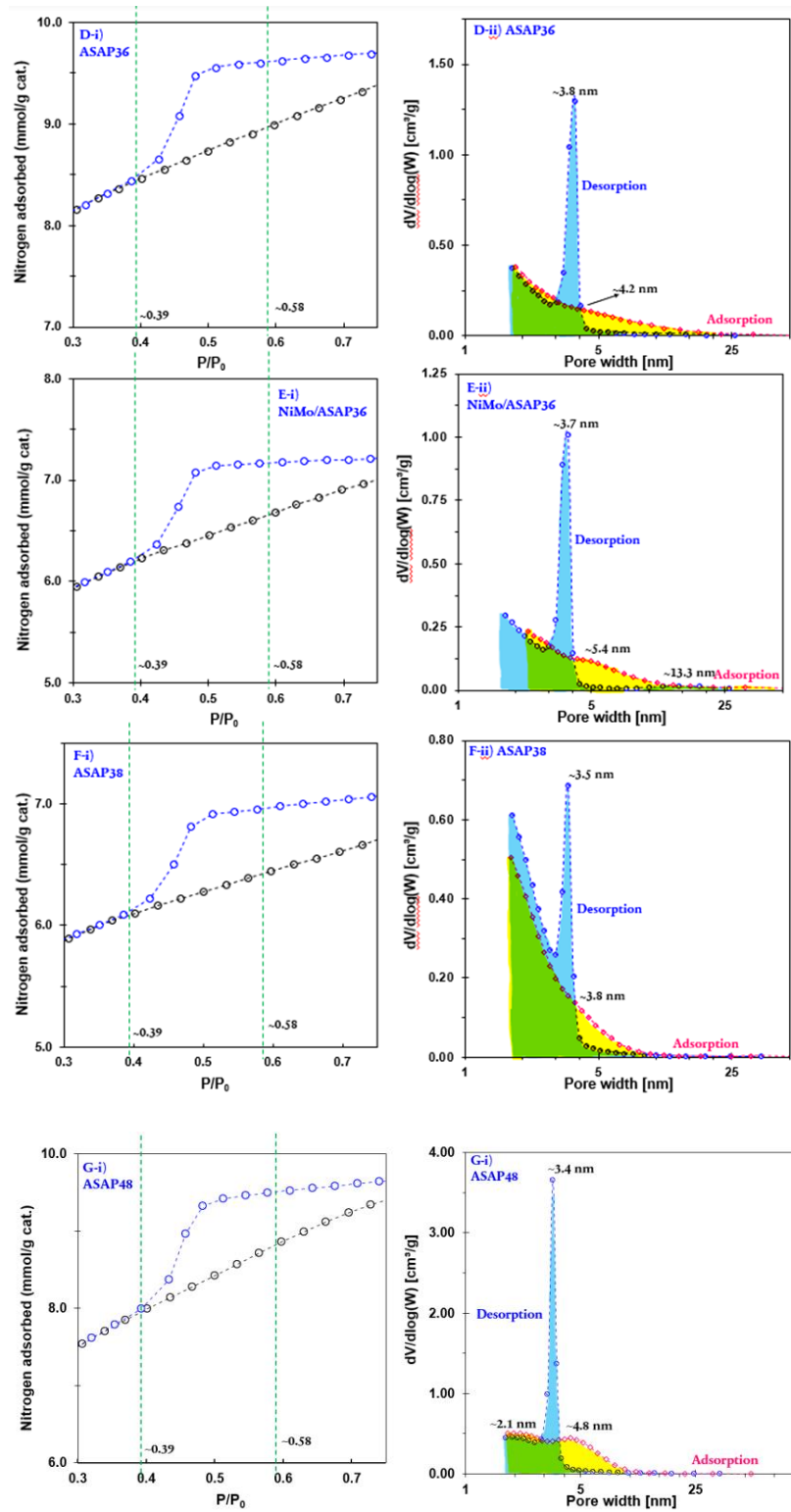


Figure 6. Continuation.

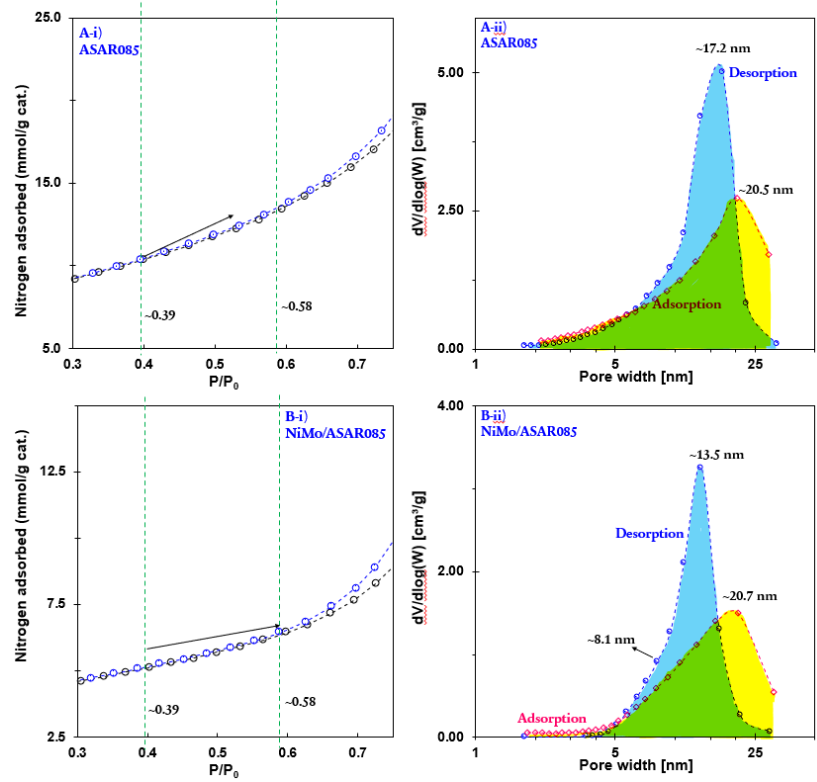


Figure 7. Details of the closure of the hysteresis loops for selected samples exhibiting IV(a) isotherms with H1(a) hysteresis loop and pore size distributions as estimated from both the adsorption and the desorption branches of the isotherms by using the BJH method⁶ with the Harkins and Jura standard isotherm¹⁰ and the Faas correction.

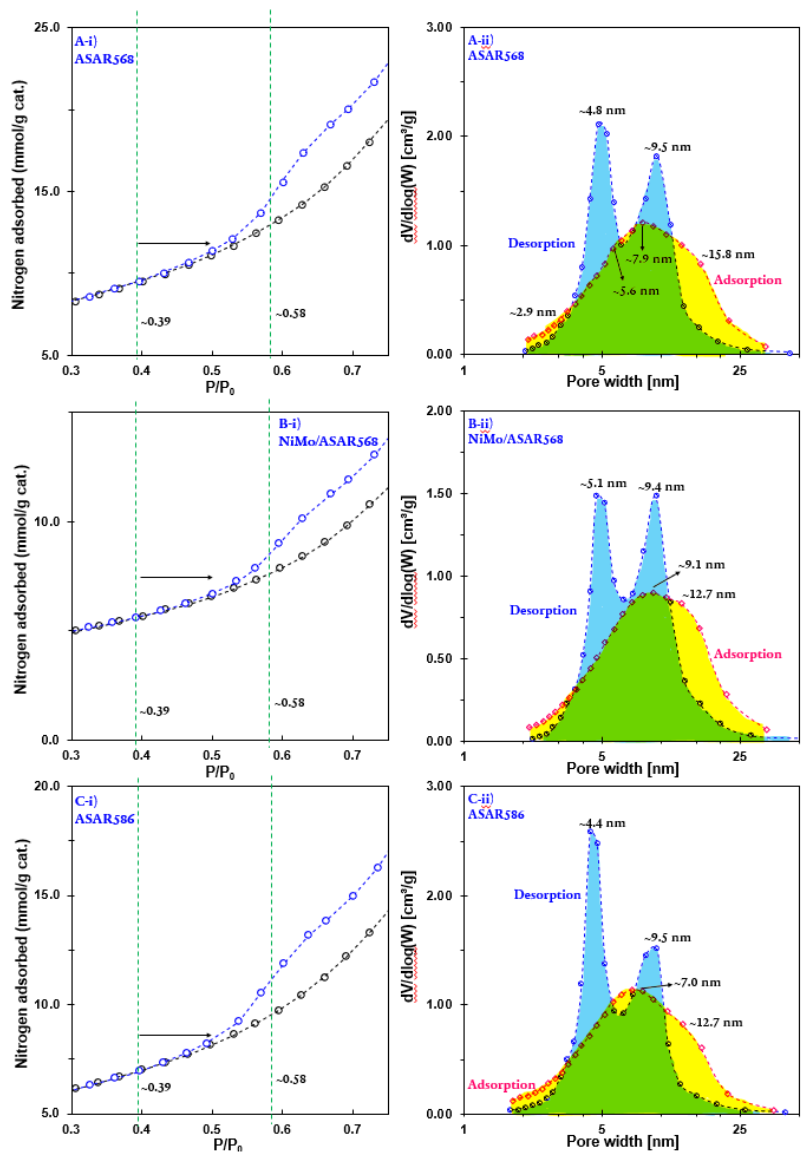


Figure 8. Details of the closure of the hysteresis loops for selected samples exhibiting IV(a) isotherms with H1(b) hysteresis loop and pore size distributions as estimated from both the adsorption and the desorption branches of the isotherms by using the BJH method⁶ with the Harkins and Jura standard isotherm¹⁰ and the Faas correction.

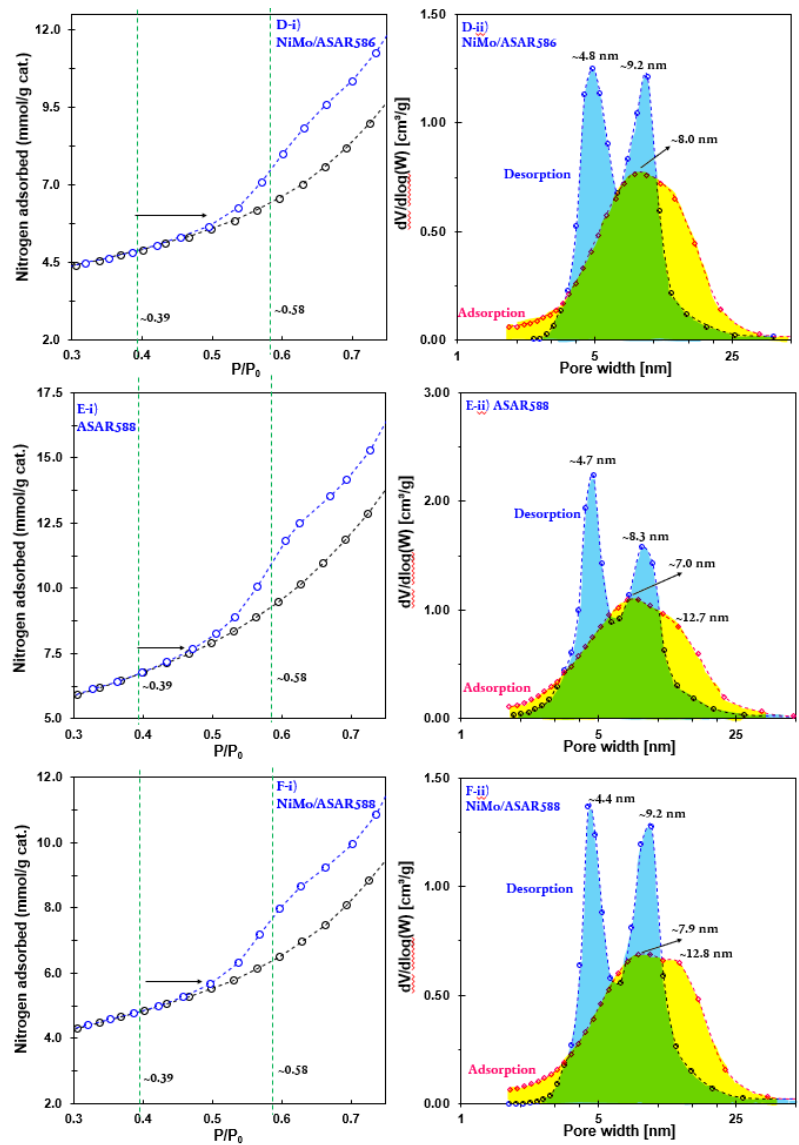


Figure 8. Continuation.

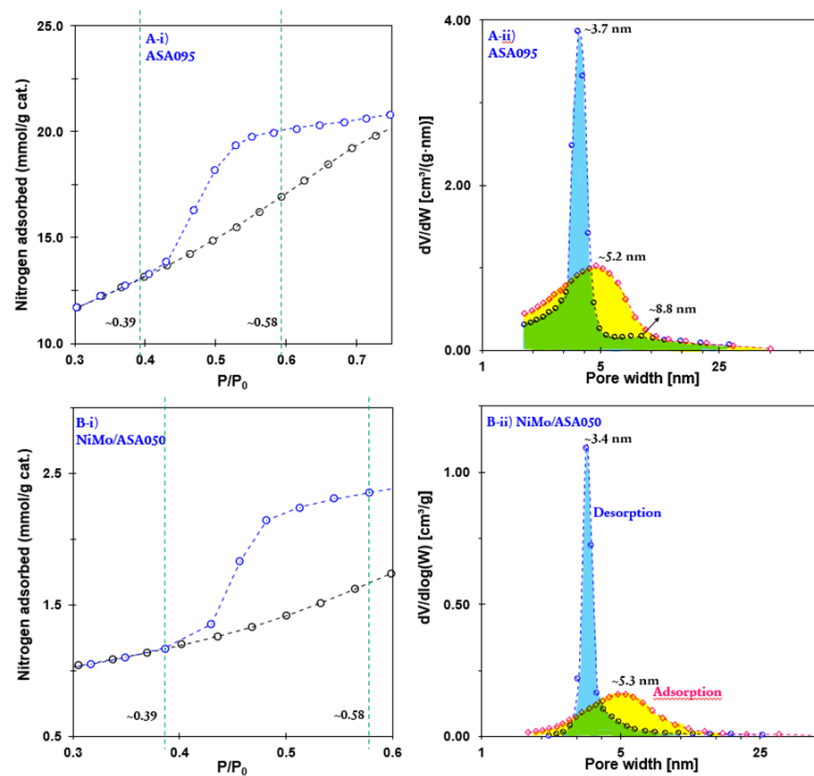


Figure 9. Details of the closure of the hysteresis loops for selected samples exhibiting IV(a) isotherms with H2(c) hysteresis loop and pore size distributions as estimated from both the adsorption and the desorption branches of the isotherms by using the BJH method⁶ with the Harkins and Jura standard isotherm¹⁰ and the Faas correction.

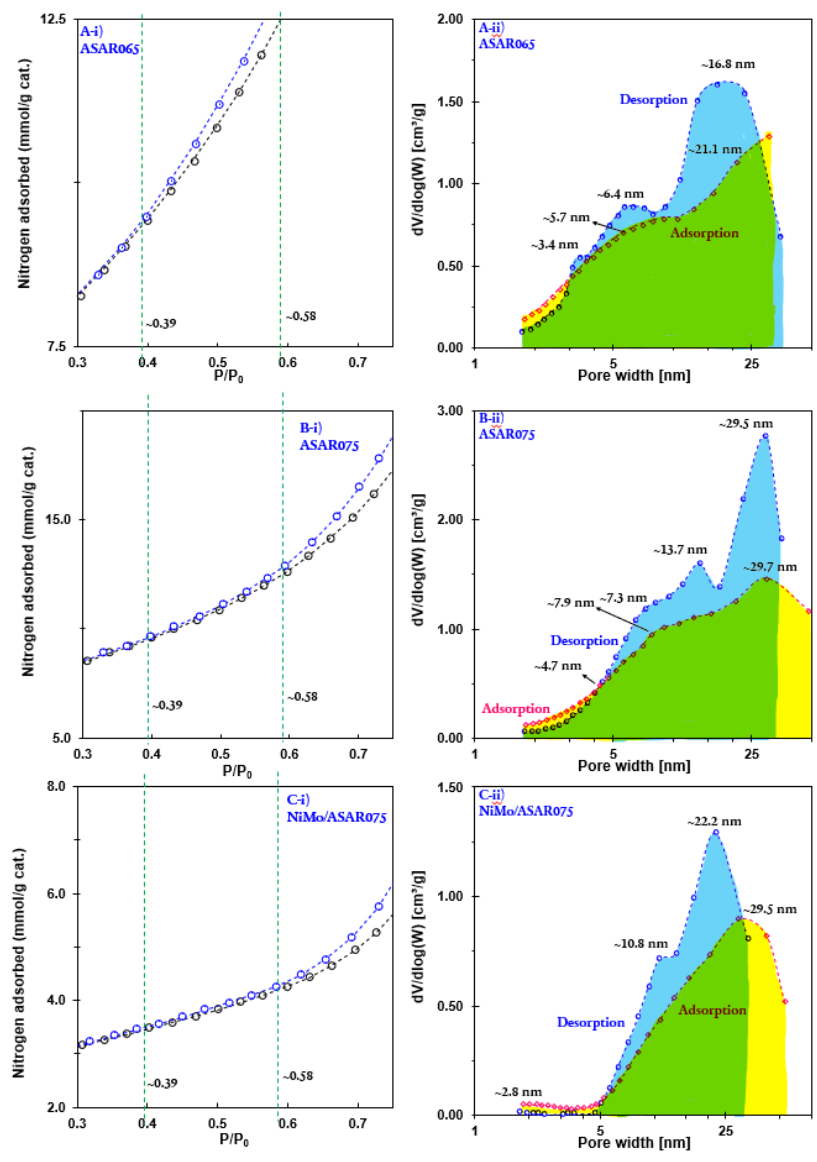


Figure 10. Details of the closure of the hysteresis loops for selected samples exhibiting IV(c) isotherms with H3(a) hysteresis loop and pore size distributions as estimated from both the adsorption and the desorption branches of the isotherms by using the BJH method⁶ with the Harkins and Jura standard isotherm¹⁰ and the Faas correction.

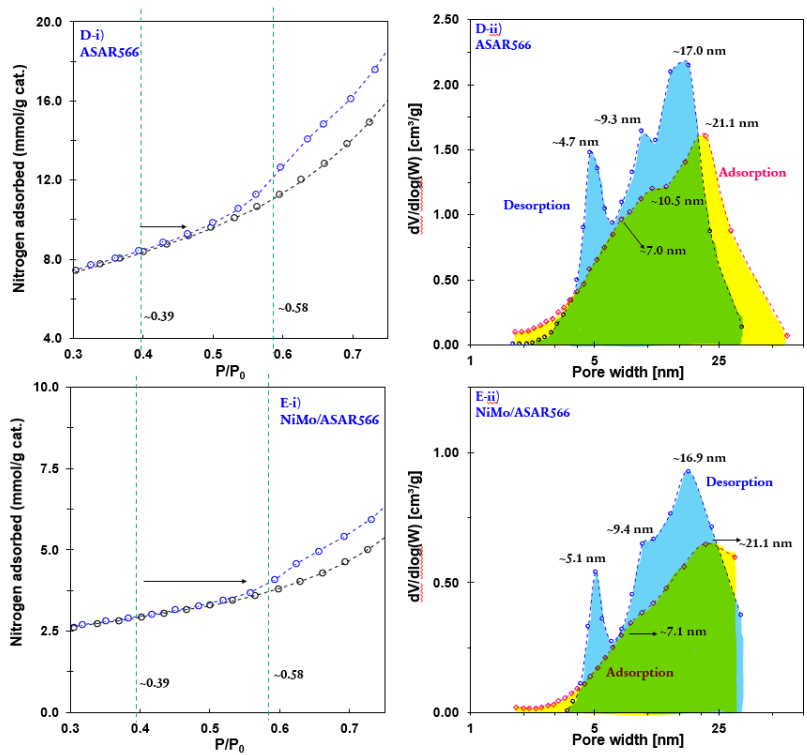


Figure 10. Continuation.

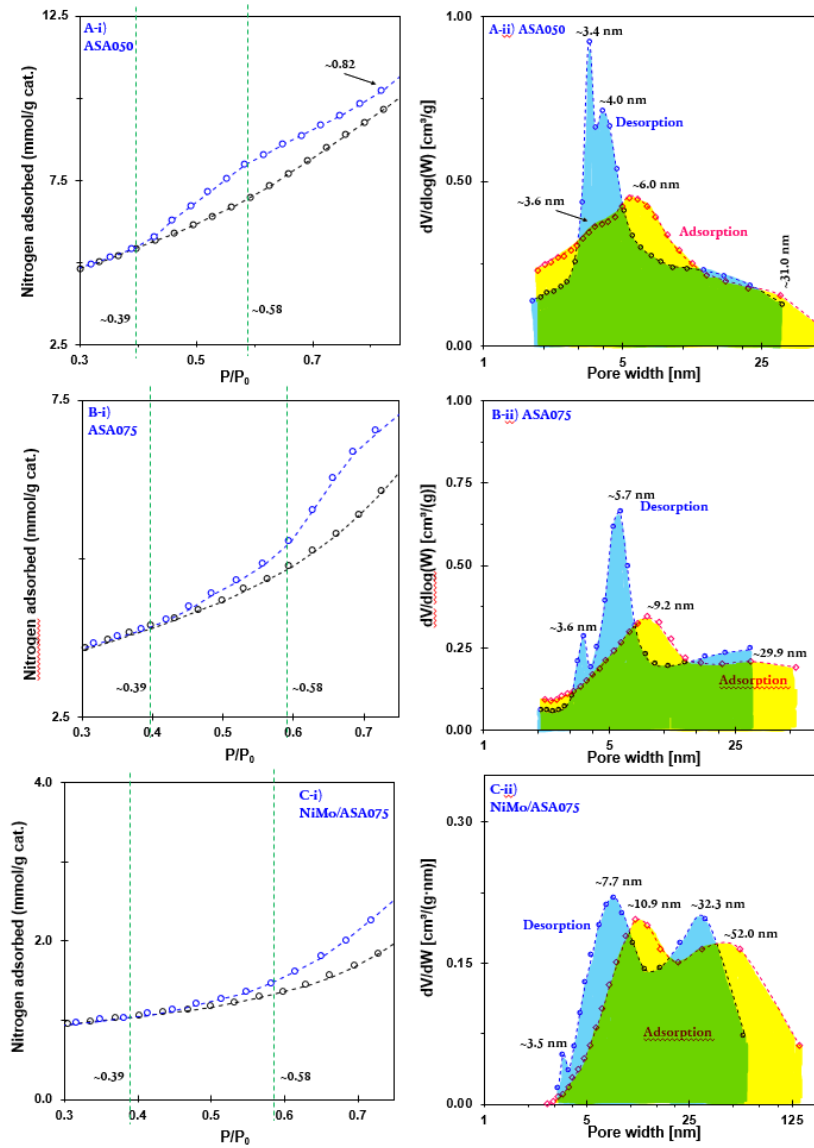


Figure 11. Details of the closure of the hysteresis loops for selected samples exhibiting IV(c) isotherms with H3(b) hysteresis loop and pore size distributions as estimated from both the adsorption and the desorption branches of the isotherms by using the BJH method⁶ with the Harkins and Jura standard isotherm¹⁰ and the Faas correction.

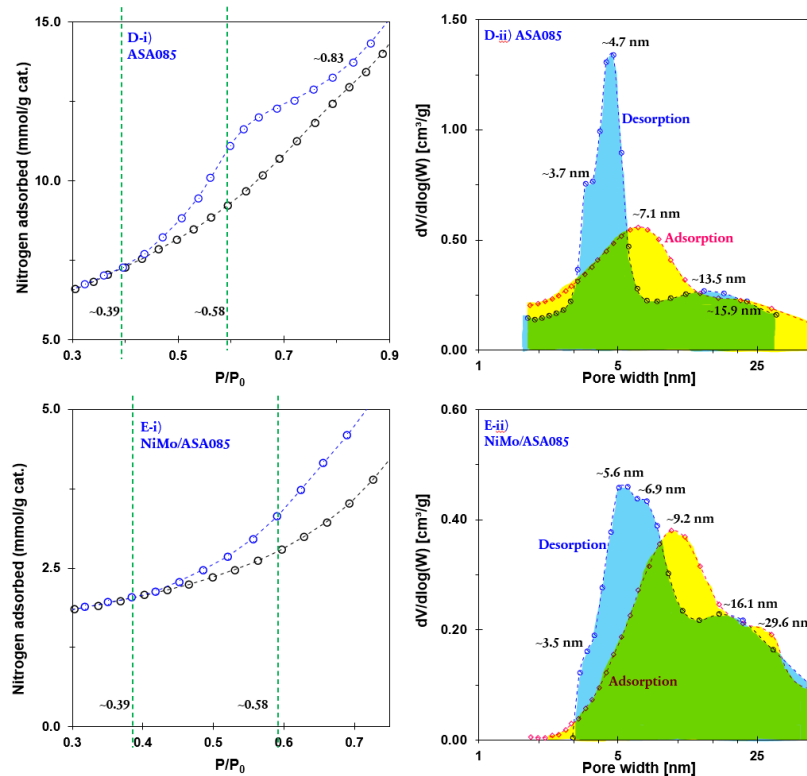


Figure 11. Continuation.

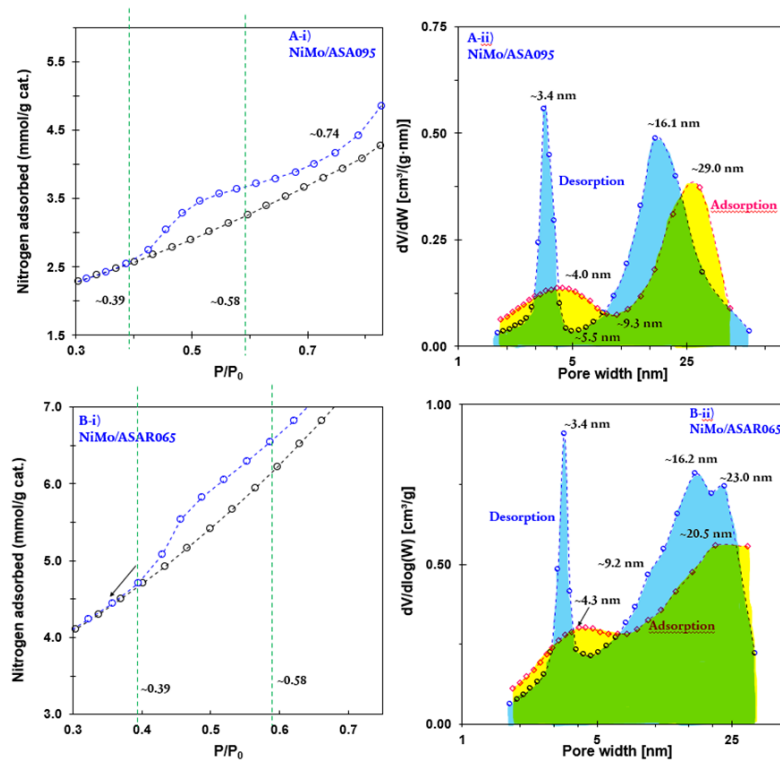


Figure 12. Details of the closure of the hysteresis loops for selected samples exhibiting IV(c) isotherms with H3(c) hysteresis loop and pore size distributions as estimated from both the adsorption and the desorption branches of the isotherms by using the BJH method⁶ with the Harkins and Jura standard isotherm¹⁰ and the Faas correction.

The pore size distributions estimated from the desorption branch of the isotherm for materials with IV(a) isotherms with H1(b) hysteresis loops, **Figure 8**, also showed strong differences with those calculated from the adsorption branch. Particularly, the pore size distributions estimated from the desorption branch were bimodal while those calculated from the adsorption branch had high symmetry around a central point; in other words, they can be represented by a Gaussian curve from which statistical normal distributions stem. In addition, the distributions derived from the adsorption branch of the isotherms always indicated that the relative number of pores of sizes larger than 10.0 nm was higher than those predicted by the distributions derived from the desorption branch. The bimodality of the pore size distributions obtained from the desorption branch hints to the strong influence of pore network effects related to cavitation by the tensile strength effect; this time occurring at $P/P_0 \approx 0.5$, and also maybe to percolation effects. In the case of the type IV(a) isotherms with H1(a) hysteresis, **Figure 7**, no peaks associated to network effects were found for the pore size distributions calculated from the desorption branch of the isotherms. Instead, a single broad and left skewed peak was found for these materials with both the adsorption and the desorption branches of the isotherm. The corresponding distributions showed that these materials mostly had large mesopores with widths larger than 13 nm.

Table 3. Description of the mesopore size distribution from the materials exhibiting a I(c) isotherm with H4(a) hysteresis loop. Distributions were calculated from the adsorption and desorption branches of the isotherms by the BJH method⁶ with the Harkins and Jura standard isotherm¹⁰ and the Faas correction.

Material code	Adsorption pore size distribution	Desorption pore size distribution
ASAP18	The curve markedly decreased in the beginning. Afterwards, the curve was almost flat with a very broad shoulder at 6.7 nm.	The curve markedly decreased in the beginning. The only peak of the distribution was the TSE peak at 3.9 nm. It was very sharp.
NiMo/ASAP18	The curve markedly decreased in the beginning. Afterwards, it was almost flat with two very broad shoulders at 8.4 and 31.9 nm.	The curve markedly decreased in the beginning. The only very sharp peak of the distribution was the TSE peak at 3.7 nm. A very broad shoulder appeared at 31.9 nm.
ASAP28	The curve decreased monotonically with a hitch at 2.8 nm and shoulder at 3.6 nm.	The curve had a semi-monotonic decreasing trend broken by the very sharp TSE peak at 3.6 nm.
NiMo/ASAP38	The curve decreased monotonically and had a very broad shoulder at 8.3 nm.	The curve had a semi-monotonic decreasing trend broken by the very sharp TSE peak at 3.5 nm.

NiMo/ASAP48	The curve was almost flat. It had a wide and not very tall peak at 5.3 nm and a shoulder at 27.8 nm.	The distribution was almost flat with a very slight decrease in the beginning. The TSE peak was very sharp, and it was centered at 3.7 nm. A very broad shoulder appeared at 15.1 nm.
-------------	--	---

Table 4. Description of the mesopore size distribution from the materials exhibiting a I(c) isotherm with H4(b) hysteresis loop. Distributions were calculated from the adsorption and desorption branches of the isotherms by the BJH method⁶ with the Harkins and Jura standard isotherm¹⁰ and the Faas correction.

Material code	Adsorption pore size distribution	Desorption pore size distribution
ASAP26	The curve decreased monotonically and had a shallow and very broad shoulder at 4.6 nm.	The curve had a semi-monotonic decreasing trend broken by the very sharp TSE peak at 3.9 nm followed by a shallow and broad shoulder at 13.4 nm.
NiMo/ASAP26	The curve decreased monotonically and had a shallow and very broad shoulder at 6.0 nm.	The curve had a semi-monotonic decreasing trend broken by the very sharp TSE peak at 3.8 nm followed by a shallow and broad shoulder at 13.3 nm.
NiMo/ASAP28	The curve was flat in the beginning. Then, it dropped monotonically at 3.8 nm.	The curve was flat in the beginning and then the very sharp TSE peak appeared at 3.6 nm.
ASAP36	The curve decreased monotonically and had a very shallow and broad shoulder at 4.2 nm.	The curve had a semi-monotonic decreasing trend broken by the very sharp TSE peak at 3.8 nm.
NiMo/ASAP36	The curve decreased monotonically and had a shallow and very broad shoulder at 5.4 nm.	The curve had a semi-monotonic decreasing trend broken by the very sharp TSE peak at 3.7 nm. A shallow and very broad shoulder appeared at 13.3 nm.
ASAP38	The curve decreased strongly and monotonically. It had a very shallow and broad shoulder at 3.8 nm.	The curve decreased strongly and had a semi-monotonic trend broken by the very sharp TSE peak at 3.5 nm.

ASAP48	The curve was almost flat. It had a very shallow peak at 2.2 nm followed by less shallow one at 5.3 nm. It ended with a shoulder at 27.8 nm.	The curve very slightly decreased before the appearance of the TSE peak at 3.7 nm. Afterwards, it showed a broad shoulder at 15.1 nm.
--------	--	---

Table 5. Description of the mesopore size distribution from the materials exhibiting a IV(a) isotherm with H1(a) hysteresis loop (marked with *), a IV(a) isotherm with H2(c) hysteresis loop (materials marked with **), and a IV(c) isotherm with H3(c) hysteresis loop. Distributions were calculated from the adsorption and desorption branches of the isotherms by the BJH method⁶ with the Harkins and Jura standard isotherm¹⁰ and the Faas correction.

Material code	Adsorption pore size distribution	Desorption pore size distribution
ASAR085*	Monotonic increasing and strongly skewed to the left distribution with incomplete peak at 20.5 nm.	Monotonically increasing and strongly skewed to the left distribution with a well-defined broad peak at 17.2 nm.
NiMo/ASAR085*	The curve was flat in the beginning. Then, it showed a strongly skewed to the left incomplete peak at 20.7 nm.	The curve was flat in the beginning. Then, it showed a strongly skewed to the left peak with a shoulder at 8.1 nm and a maximum at 13.5 nm.
NiMo/ASA050**	Distribution with high symmetry around the center which was located at 5.3 nm.	The distribution was skewed to the right with a very sharp TSE peak at 3.4 nm.
ASA095**	The curve was skewed to the left and centered at 5.2 nm.	The distribution was skewed to the left with a very sharp TSE peak at 3.7 nm. It showed a shallow and broad peak at 8.8 nm.
NiMo/ASA095***	The distribution showed two relatively symmetric broad and well separated peaks. The tallest was at 29.0 nm and the other was located at 4.0 nm. Peaks were separated by a deep valley near 9.3 nm.	A sharp TSE peak at 3.4 nm followed by relatively smaller and broader peak at 16.1 nm. The valley between the peaks was deep and around 5.5 nm. Both peaks showed weak skewness to the left.
NiMo/ASAR065***	The curve increased monotonically and showed a broad peak at 4.3 nm followed by an inflection point at 20.5 nm.	The curve increased monotonically and showed the TSE peak at 3.4 nm. A second very broad peak was composed of a shoulder at 9.2 nm, a

maximum at 16.2 nm, and a hitch at 23.0 nm.

Table 6. Description of the mesopore size distribution from the materials exhibiting a IV(c) isotherm with H3(a) hysteresis loop. Distributions were calculated from the adsorption and desorption branches of the isotherms by the BJH method⁶ with the Harkins and Jura standard isotherm¹⁰ and the Faas correction.

Material code	Adsorption pore size distribution	Desorption pore size distribution
ASAR065*	The curve increased monotonically and showed a very broad and relatively shallow peak at 5.7 nm. Afterwards, it showed an inflection point at 21.1 nm.	The curve increased monotonically and showed the TSE peak as a bump at 3.4 nm. The latter was followed by a skewed to the left broad peak at 6.4 nm. The curve then showed a very wide peak at 16.8 nm.
ASAR075*	The curve started flat and showed a single incomplete and very broad peak that had a hitch at 4.7 nm, a shoulder at 7.9 nm, and a maximum at 29.7 nm.	The curve started flat and then showed two peaks. The first peak showed a shoulder at 7.3 nm followed by its maximum at 13.7 nm. The second peak was incomplete, skewed to the left, and relatively narrow with a pointy maximum at 29.5 nm. There was a small valley between the two peaks.
NiMo/ASAR075*	The curved showed a shallow hitch at 2.8 nm. Then, a very broad peak, incomplete, and skewed to the left peak appeared with a maximum at 29.5 nm.	The curve slightly decreased in the beginning. Then, a broad incomplete peak appeared showing a flat shoulder at 10.8 nm and a pointy maximum at 22.2 nm.
ASAR566*	The curve resembled a mountain with a short plateau at 10.5 nm and a point summit at 21.1 nm.	The curver resembled a chain of three mountains with the sharp TSE peak at 4.7 nm and a second pointy peak at 9.3 nm. The summit was at 17.0 nm.
NiMo/ASAR566*	The curve showed a single incomplete and very broad peak with a shoulder at 7.1 nm and a maximum at 21.1 nm.	The curve resembled a mountain chain with the TSE peak at 5.1 nm, a short plateau at 9.4 nm, and a pointy summit at 16.9 nm.

Table 7. Description of the mesopore size distribution from the materials exhibiting a IV(a) isotherm with H1(b) hysteresis loop. Distributions were calculated from the adsorption and desorption branches of the isotherms by the BJH method⁶ with the Harkins and Jura standard isotherm¹⁰ and the Faas correction.

Material code	Adsorption pore size distribution	Desorption pore size distribution
ASAR568	The distribution showed a single, relatively symmetric, and very broad peak with a shallow sag at 2.9 nm, a hitch at 5.6 nm, a summit at 7.9 nm, and a shoulder at 15.8 nm.	The distribution showed two relatively symmetric peaks separated by a valley. The first and tallest peak showed its maximum at 4.8 nm, while the second peak had its summit at 9.5 nm.
NiMo/ASAR568	The distribution showed a single, symmetric and very broad peak with a maximum at 9.1 nm and a shallow shoulder at 12.7 nm.	The distribution showed two symmetric peaks of approximately the size height and separated by a valley. The first peak showed its maximum at 5.1 nm, while the second had its summit at 9.4 nm.
ASAR586	The distribution showed a single and very broad peak with a maximum at 7.0 nm and a shallow shoulder at 12.7 nm.	The distribution showed two peaks. The first and tallest was the TSE peak at 4.4 nm and the second at 9.5 nm.
NiMo/ASAR586	The distribution showed a single, symmetric and very broad peak with a maximum at 8.0 nm.	The distribution showed two symmetric peaks of approximately the same size height and separated by a valley. The first peak was the TSE at 4.8 nm and the second was at 9.2 nm.
ASAR588	The distribution showed a single, relatively symmetric, and very broad peak with a maximum at 7.0 nm and a shallow shoulder at 12.7 nm.	The distribution showed two relatively symmetric peaks separated by a valley. The first and tallest peak was the TSE at 4.7 nm and the second was at 8.3 nm.
NiMo/ASAR588	The distribution showed a single, relatively symmetric and very broad peak with a maximum at 7.9 nm and a shoulder at 12.8 nm.	The distribution showed two relatively symmetric peaks of approximately the same height and separated by a valley. The first and tallest peak was the TSE at 4.4 nm and the second was at 9.2 nm.

Table 8. Description of the mesopore size distribution from the materials exhibiting a IV(c) isotherm with H3(b) hysteresis loop. Distributions were calculated from the adsorption and desorption branches of the isotherms by the BJH method⁶ with the Harkins and Jura standard isotherm¹⁰ and the Faas correction.

Material code	Adsorption pore size distribution	Desorption pore size distribution
ASA050	Very broad and skewed to the left with shoulder at 3.6 nm, main peak at 6.0 nm, and shoulder at 31.0 nm.	Very sharp TSE peak at 3.4 nm followed by smaller narrow peak at 4.0 nm. The peaks show weak skewness.
ASA075	The curve decreased slightly in the beginning. The distribution was very broad and skewed to the left with one main peak at 9.2 nm and shoulder at 29.9 nm.	The curve slightly decreased in the beginning. There was a sharp TSE peak at 3.6 nm followed by taller wide peak at 5.7 nm and very wide shoulder at 29.9 nm. Peaks were skewed to the left.
NiMo/ASA075	The distribution showed two broad peaks. The tallest was at 10.9 nm and the other was the broadest and it was located at 52.0 nm. Peaks were separated by a shallow valley. The second peak was strongly skewed to the left.	Small TSE peak (hitch) at 3.5 nm followed by tallest broad peak 7.7 nm and then by a smaller broader peak at 32.3 nm. The peaks were well separated by a valley. The second peak showed the strongest skewness to the left.
ASA085	The distribution showed a single very broad, semi-symmetric peak at 7.1 nm followed by a smaller shoulder at 15.9 nm	The curve showed a very slight decrease in the beginning. The TSE peak appeared as a flat shoulder at 3.7 nm followed by a weakly skewed peak at 4.7 nm and then by a very broad peak at 13.5 nm. The two main peaks were separated by a very shallow valley.
NiMo/ASA085	Very broad and weakly skewed distribution. The main peak appears at 9.2 nm followed by a strong shoulder 29.6 nm.	Very broad distribution. TSE appears at 3.5 nm as a shoulder of the tallest peak whose maximum is at 5.6 nm. The latter is weakly skewed and is followed by another shoulder at 6.9 nm which is almost at the same height as the top of the distribution. The smallest peak appears at 16.1 nm and is separated by shallow valley from the main peak.

Concerning the pore size distributions for those materials showing IV(c) type isotherms, **Figures 10 to 12**, though network effects were found to influence the distributions

calculated from the desorption branch of the isotherms, in this case, the shapes of the curves found from the adsorption branch showed better resemblance to those from the desorption branch. Hence, pore size distributions from both branches of the isotherm were multimodal.

The findings described above demonstrated the complexity of the pore networks that amorphous aluminosilicates can develop. Another metric that may help analyzing such a complexity is the fractal dimension. Herein, plotting the fractal dimension as a function of the BET surface area, **Figure S4** and the percentage of microporosity, **Figure S5**, of the studied materials led to no apparent correlations. Therefore, it was decided to analyze how the fractal dimension behaved when considering the different types of isotherms and hysteresis loops showed by the tested amorphous aluminosilicates. **Figure 13** presents boxplots for the fractal dimension as function of the type of hysteresis loop and isotherm. It was found that the fractal dimension tended to increase for those hysteresis loops that represented more complex pore networks from materials showing type I(c) and IV(a) isotherms. Meanwhile, the opposite seemed to be true for those materials with a type IV(c) isotherm. At present, no further conclusions can be drawn from the current measurements.

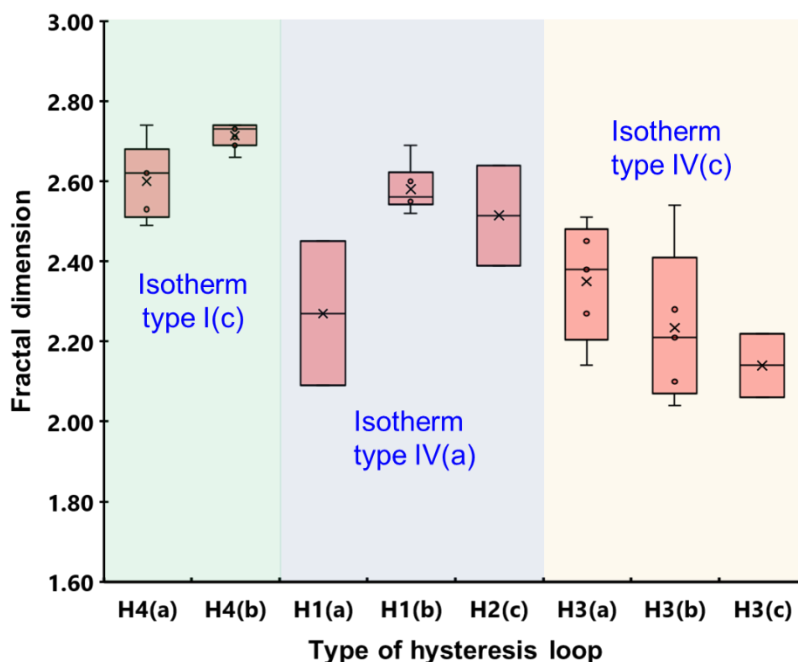


Figure 13. Boxplots correlating the fractal dimension of the studied materials and the corresponding type of hysteresis loop for each one of the types of isotherms identified herein. Fractal dimensions were estimated with the method of Sandoval et al.⁶⁰

5. Conclusions

This paper presented a systematic analysis of the nitrogen physisorption data measured for a series amorphous aluminosilicates. The analysis started with an ample description of the features of the recorded isotherms. This was made with the purpose of identifying the nature of the porous networks of the materials. To do this, the isotherms and hysteresis loops recorded for the different materials were classified following IUPAC recommendations. However, it was found that several materials could not be described by

the standard isotherms and hysteresis loops of the IUPAC classification. Therefore, two new types of isotherms, types I(c) and IV(c), and five new types of hysteresis loops, H1(b), H2(c), H3(b), H3(c), and H4(b), were proposed to better describe these materials. The need for these classifications stemmed from the microporous – mesoporous nature of the materials and from the presence of strong network effects. The exercise of describing and classifying the isotherms helped interpreting and judging the results of the calculations made with classic methods to assess the texture of the materials; namely, their total surface area by the BET method, microporous surface area by the t-plot method, mesopore size distribution by the BJH method, and fractal dimension by the method proposed by Sandoval et al.⁶⁰ From these results, it was possible to establish the following: (i) for microporous – mesoporous materials, there is an exponential type correlation between the physisorption energy (herein indirectly and qualitatively assessed with the C_{BET} constant) and the relative percentage of microporosity. (ii) A better assessment of the mesopore size distributions derived from the BJH method is done by comparing the results obtained with both branches of the isotherms and when systematically classifying the recorded isotherms before. (iii) The fractal dimension is a useful complementary descriptor of the complexity of the porous network of the material as long as the classification of the materials is based on the corresponding types of isotherms and hysteresis loops guide the analysis.

Acknowledgements

V.G. Baldovino-Medrano thanks funding from the Instituto Colombiano del Petróleo (ICP) and Universidad Industrial de Santander -UIS- Specific cooperation project No. 5219040 and from Agencia Nacional de Hidrocarburos –ANH– and Minciencias, Colombia, within the frame of the Project 110284769842: “Desarrollo de una estrategia catalítica para un proceso de in-situ upgrading acoplado con procesos de combustión in-situ para optimizar la producción y mejorar la calidad de crudos pesados y extrapesados colombianos por reacciones de transferencia de hidrógeno”. Authors thank MSc. Eng. Angélica Coconubo and MSc. Eng. María Mercedes Duarte for performing the physisorption tests featured in this work. We also thank Ph.D. student Eng. Julieth Tatiana García Sánchez for coloring.

References

- (1) Sing, K. The Use of Nitrogen Adsorption for the Characterisation of Porous Materials. *Colloids Surfaces A Physicochem. Eng. Asp.* **2001**, 187–188, 3–9. [https://doi.org/https://doi.org/10.1016/S0927-7757\(01\)00612-4](https://doi.org/https://doi.org/10.1016/S0927-7757(01)00612-4).
- (2) Sing, K. S. W. Adsorption Methods for the Characterization of Porous Materials. *Adv. Colloid Interface Sci.* **1998**, 76–77, 3–11. [https://doi.org/https://doi.org/10.1016/S0001-8686\(98\)00038-4](https://doi.org/https://doi.org/10.1016/S0001-8686(98)00038-4).
- (3) Langmuir, I. The Constitution and Fundamental Properties of Solids and Liquids. Part I. Solids. *J. Am. Chem. Soc.* **1916**, 38 (11), 2221–2295. <https://doi.org/10.1021/ja02268a002>.
- (4) Brunauer, S.; Emmett, P. H.; Teller, E. Adsorption of Gases in Multimolecular Layers. *J. Am. Chem. Soc.* **1938**, 60 (2), 309–319. <https://doi.org/10.1021/ja01269a023>.
- (5) Shull, C. G.; Elkin, P. B.; Roess, L. C. Physical Studies of Gel Microstructure. *J. Am. Chem. Soc.* **1948**, 70 (4), 1410–1414. <https://doi.org/10.1021/ja01184a035>.
- (6) Barrett, E. P.; Joyner, L. G.; Halenda, P. P. The Determination of Pore Volume and

- Area Distributions in Porous Substances. I. Computations from Nitrogen Isotherms. *J. Am. Chem. Soc.* **1951**, *73* (1), 373–380. <https://doi.org/10.1021/ja01145a126>.
- (7) Sing, K. S. W.; Everett, D. H.; Haul, R. A. W.; Moscou, L.; Pierotti, R. A.; Rouquerol, J.; Siemieniewska, T. Reporting Physisorption Data for Gas/Solid Systems with Special Reference to the Determination of Surface Area and Porosity (Recommendations 1984). *Pure Appl. Chem.* **1985**, *57* (4), 603–619. <https://doi.org/doi:10.1351/pac198557040603>.
 - (8) Dubinin, M. M. A Study of the Porous Structure of Active Carbons Using a Variety of Methods. *Q. Rev. Chem. Soc.* **1955**, *9* (2), 101–114. <https://doi.org/10.1039/QR9550900101>.
 - (9) Harkins, W. D.; Jura, G. Surfaces of Solids. XIII. A Vapor Adsorption Method for the Determination of the Area of a Solid without the Assumption of a Molecular Area, and the Areas Occupied by Nitrogen and Other Molecules on the Surface of a Solid. *J. Am. Chem. Soc.* **1944**. <https://doi.org/10.1021/ja01236a048>.
 - (10) Harkins, W. D.; Jura, G. An Adsorption Method for the Determination of the Area of a Solid without the Assumption of a Molecular Area, and the Area Occupied by Nitrogen Molecules on the Surfaces of Solids. *J. Chem. Phys.* **1943**, *11* (9), 431–432. <https://doi.org/10.1063/1.1723871>.
 - (11) Gregg, S. J.; Sing, K. S. W. *Adsorption, Surface Area and Porosity*, 1st editio.; Academic Press: London, 1967; Vol. 63.
 - (12) Rouquerol, F.; Rouquerol, J.; Sing, K. S. W.; Llewellyn, P.; Maurin, G. *Adsorption by Powders and Porous Solids*; 2014. <https://doi.org/10.1017/CBO9781107415324.004>.
 - (13) Saito, A.; Foley, H. C. Curvature and Parametric Sensitivity in Models for Adsorption in Micropores. *AIChE J.* **1991**, *37* (3), 429–436. <https://doi.org/https://doi.org/10.1002/aic.690370312>.
 - (14) Kaneko, K. Determination of Pore Size and Pore Size Distribution: 1. Adsorbents and Catalysts. *J. Memb. Sci.* **1994**, *96* (1), 59–89. [https://doi.org/https://doi.org/10.1016/0376-7388\(94\)00126-X](https://doi.org/https://doi.org/10.1016/0376-7388(94)00126-X).
 - (15) Landers, J.; Gor, G. Y.; Neimark, A. V. Density Functional Theory Methods for Characterization of Porous Materials. *Colloids Surfaces A Physicochem. Eng. Asp.* **2013**, *437*, 3–32. <https://doi.org/https://doi.org/10.1016/j.colsurfa.2013.01.007>.
 - (16) Rigby, S. P.; Chigada, P. I.; Perkins, E. L.; Watt-Smith, M. J.; Lowe, J. P.; Edler, K. J. Fundamental Studies of Gas Sorption within Mesopores Situated amidst an Inter-Connected, Irregular Network. *Adsorption* **2008**, *14* (2), 289–307. <https://doi.org/10.1007/s10450-007-9091-8>.
 - (17) Rouquerol, J.; Llewellyn, P.; Rouquerol, F. Is the Bet Equation Applicable to Microporous Adsorbents? *Stud. Surf. Sci. Catal.* **2007**, *160*, 49–56. [https://doi.org/10.1016/S0167-2991\(07\)80008-5](https://doi.org/10.1016/S0167-2991(07)80008-5).
 - (18) Schneider, P. Adsorption Isotherms of Microporous-Mesoporous Solids Revisited. *Appl. Catal. A Gen.* **1995**, *129* (2), 157–165. [https://doi.org/https://doi.org/10.1016/0926-860X\(95\)00110-7](https://doi.org/https://doi.org/10.1016/0926-860X(95)00110-7).
 - (19) Storck, S.; Bretinger, H.; Maier, W. F. Characterization of Micro- and Mesoporous Solids by Physisorption Methods and Pore-Size Analysis. *Appl. Catal. A Gen.* **1998**, *174* (1), 137–146. [https://doi.org/https://doi.org/10.1016/S0926-860X\(98\)00164-1](https://doi.org/https://doi.org/10.1016/S0926-860X(98)00164-1).
 - (20) Donohue, M. D.; Aranovich, G. L. Classification of Gibbs Adsorption Isotherms. *Adv. Colloid Interface Sci.* **1998**, *76–77*, 137–152. [https://doi.org/https://doi.org/10.1016/S0001-8686\(98\)00044-X](https://doi.org/https://doi.org/10.1016/S0001-8686(98)00044-X).

- (21) Jaroniec, M.; Choma, J.; Kruk, M. On the Applicability of the Horwath-Kawazoe Method for Pore Size Analysis of MCM-41 and Related Mesoporous Materials. In *Characterisation of Porous Solids V*; Unger, K. K., Kreysa, G., Baselt, J. P. B. T.-S. in S. S. and C., Eds.; Elsevier, 2000; Vol. 128, pp 225–234. [https://doi.org/https://doi.org/10.1016/S0167-2991\(00\)80026-9](https://doi.org/https://doi.org/10.1016/S0167-2991(00)80026-9).
- (22) Groen, J. C.; Peffer, L. A. A.; Pérez-Ramírez, J. Pore Size Determination in Modified Micro- and Mesoporous Materials. Pitfalls and Limitations in Gas Adsorption Data Analysis. *Microporous Mesoporous Mater.* **2003**, *60* (1), 1–17. [https://doi.org/https://doi.org/10.1016/S1387-1811\(03\)00339-1](https://doi.org/https://doi.org/10.1016/S1387-1811(03)00339-1).
- (23) Rouquerol, F.; Sing, K.; Rouquerol, J. *Adsorption by Powders and Porous Solids*, 1st editio.; Academic Press: London, 1999. <https://doi.org/https://doi.org/10.1016/B978-0-12-598920-6.X5000-3>.
- (24) Condon, J. B. *Surface Area and Porosity Determinations by Physisorption Measurements and Theory*, 1st ed.; Elsevier Science: Amsterdam, 2006.
- (25) Lowell, S.; Shields, J. E.; Thomas, M. A.; Thommes, M. Characterization of Porous Solids and Powders-Surface Area, Pore Size and Density. *Part. Technol. Ser.* **2004**, *16*, 157–188. <https://doi.org/10.1007/978-1-4020-2303-3>.
- (26) Schüth, F.; Sing, K. S. W.; Weitkamp, J. *Handbook of Porous Solids*, 1st ed.; Schüth, F., Sing, K. S. W., Weitkamp, J., Eds.; Wiley-VCH Verlag & Co.: Berlin, 2002.
- (27) Thommes, M.; Cychosz, K. A. Physical Adsorption Characterization of Nanoporous Materials: Progress and Challenges. *Adsorption* **2014**, *20* (2–3), 233–250. <https://doi.org/10.1007/s10450-014-9606-z>.
- (28) Marcilla, A.; Gomez-Siurana, A.; José, M. M.; Valdés, F. J. Comments on the Methods of Characterization of Textural Properties of Solids from Gas Adsorption Data. *Adsorpt. Sci. Technol.* **2009**, *27* (1), 69–84. <https://doi.org/10.1260/026361709788921579>.
- (29) Bardestani, R.; Patience, G. S.; Kaliaguine, S. Experimental Methods in Chemical Engineering: Specific Surface Area and Pore Size Distribution Measurements—BET, BJH, and DFT. *Can. J. Chem. Eng.* **2019**, *97* (11), 2781–2791. <https://doi.org/https://doi.org/10.1002/cjce.23632>.
- (30) Leofanti, G.; Padovan, M.; Tozzola, G.; Venturelli, B. Surface Area and Pore Texture of Catalysts. *Catal. Today* **1998**, *41* (1), 207–219. [https://doi.org/https://doi.org/10.1016/S0920-5861\(98\)00050-9](https://doi.org/https://doi.org/10.1016/S0920-5861(98)00050-9).
- (31) Thommes, M.; Kaneko, K.; Neimark, A. V.; Olivier, J. P.; Rodriguez-Reinoso, F.; Rouquerol, J.; Sing, K. S. W. Physisorption of Gases, with Special Reference to the Evaluation of Surface Area and Pore Size Distribution (IUPAC Technical Report). *Pure Appl. Chem.* **2015**, *87* (9–10), 1051–1069. <https://doi.org/10.1515/pac-2014-1117>.
- (32) ASTM. *ASTM-D4222 › Standard Test Method for Determination of Nitrogen Adsorption and Desorption Isotherms of Catalysts and Catalyst Carriers by Static Volumetric Measurements*; 2020.
- (33) Various. *Synthesis of Solid Catalysts*, 1st ed.; de Jong, K. P., Ed.; Wiley-VCH Verlag GmbH & Co. KGaA: Weinheim, 2009. <https://doi.org/10.1002/9783527626854>.
- (34) Campanati, M.; Fornasari, G.; Vaccari, A. Fundamentals in the Preparation of Heterogeneous Catalysts. *Catal. Today* **2003**, *77* (4), 299–314. [https://doi.org/http://dx.doi.org/10.1016/S0920-5861\(02\)00375-9](https://doi.org/http://dx.doi.org/10.1016/S0920-5861(02)00375-9).
- (35) Duarte Mantilla, M. M. Efectos de La Relación Si/(Si+Al) En La Acidez y


- Comportamiento de Catalizadores NiMo Soportados En Aluminosilicatos Amorfos (NiMo/ASA), En El Hidrocraqueo de Gasóleo de Vacío, Universidad Industrial de Santander, Bucaramanga, 2018.
- (36) Coconubo Díaz, A. M. Efecto de La Porosidad de Sílice- Alúminas Amorfos En La Actividad de Catalizadores de Hidrocraqueo, Universidad Industrial de Santander, Bucaramanga, 2018.
- (37) Busca, G. Silica-Alumina Catalytic Materials: A Critical Review. *Catal. Today* **2020**, 357, 621–629. <https://doi.org/https://doi.org/10.1016/j.cattod.2019.05.011>.
- (38) Pérez-Ramírez, J.; Verboekend, D.; Bonilla, A.; Abelló, S. Zeolite Catalysts with Tunable Hierarchy Factor by Pore-Growth Moderators. *Adv. Funct. Mater.* **2009**, 19 (24), 3972–3979. <https://doi.org/https://doi.org/10.1002/adfm.200901394>.
- (39) Hartmann, M.; Thommes, M.; Schwieger, W. Hierarchically-Ordered Zeolites: A Critical Assessment. *Adv. Mater. Interfaces* **2021**, 8 (4), 2001841. <https://doi.org/https://doi.org/10.1002/admi.202001841>.
- (40) Li, K.; Beaver, M.; Speronello, B.; García-Martínez, J. Surfactant-Templated Mesoporous Structuring of Zeolites: From Discovery to Commercialization. *Mesoporous Zeolites*. April 20, 2015, pp 321–348. <https://doi.org/https://doi.org/10.1002/9783527673957.ch10>.
- (41) García-Martínez, J.; Li, K.; Davis, M. E. *Mesoporous Zeolites: Preparation, Characterization and Applications*, 1st ed.; García-Martínez, J., Li, K., Eds.; Wiley Interscience, 2015.
- (42) La Parola, V.; Deganello, G.; Scirè, S.; Venezia, A. M. Effect of the Al/Si Atomic Ratio on Surface and Structural Properties of Sol–Gel Prepared Aluminosilicates. *J. Solid State Chem.* **2003**, 174 (2), 482–488. [https://doi.org/https://doi.org/10.1016/S0022-4596\(03\)00321-9](https://doi.org/https://doi.org/10.1016/S0022-4596(03)00321-9).
- (43) Ishihara, A.; Wakamatsu, T.; Nasu, H.; Hashimoto, T. Preparation of Amorphous Silica-Alumina Using Polyethylene Glycol and Its Role for Matrix in Catalytic Cracking of n-Dodecane. *Appl. Catal. A Gen.* **2014**, 478, 58–65. <https://doi.org/https://doi.org/10.1016/j.apcata.2014.03.016>.
- (44) Baldovino-Medrano, V.-G.; Centeno, A.; Giraldo, S.-A. Evaluating the Functionalities of NiMo/g-Al₂O₃-B₂O₃ Catalysts in Naphthalene Hydrodearomatization and Dibenzothiophene Hydrodesulfurization. *CT&F - Ciencia, Tecnología y Futuro*. scieloco 2010, pp 91–99.
- (45) Baldovino-Medrano, V. G.; Giraldo, S. A.; Centeno, A. Comportamiento de Catalizadores PtMo/g-Al₂O₃-B₂O₃ En Reacciones de Hidrodesaromatización de Naftaleno e Hidrodesulfuración de Dibenzotiofeno. *Información tecnológica*. scielocl 2009, pp 3–10.
- (46) Ardila-Suárez, C.; Molina V., D. R.; Alem, H.; Baldovino-Medrano, V. G.; Ramírez-Caballero, G. E. Synthesis of Ordered Microporous/Macroporous MOF-808 through Modulator-Induced Defect-Formation, and Surfactant Self-Assembly Strategies. *Phys. Chem. Chem. Phys.* **2020**, 22 (22), 12591–12604. <https://doi.org/10.1039/D0CP00287A>.
- (47) Yuan, S.; Zou, L.; Qin, J.-S.; Li, J.; Huang, L.; Feng, L.; Wang, X.; Bosch, M.; Alsalmé, A.; Cagin, T.; Zhou, H.-C. Construction of Hierarchically Porous Metal–Organic Frameworks through Linker Labilization. *Nat. Commun.* **2017**, 8 (1), 15356. <https://doi.org/10.1038/ncomms15356>.
- (48) Xuan, W.; Zhu, C.; Liu, Y.; Cui, Y. Mesoporous Metal–Organic Framework

- Materials. *Chem. Soc. Rev.* **2012**, *41* (5), 1677–1695. <https://doi.org/10.1039/C1CS15196G>.
- (49) Sing, K. S. W.; Williams, R. T. Physisorption Hysteresis Loops and the Characterization of Nanoporous Materials. *Adsorpt. Sci. Technol.* **2004**. <https://doi.org/10.1260/0263617053499032>.
- (50) Grosman, A.; Ortega, C. Capillary Condensation in Porous Materials. Hysteresis and Interaction Mechanism without Pore Blocking/Percolation Process. *Langmuir* **2008**, *24* (8), 3977–3986. <https://doi.org/10.1021/la703978v>.
- (51) Monson, P. A. Understanding Adsorption/Desorption Hysteresis for Fluids in Mesoporous Materials Using Simple Molecular Models and Classical Density Functional Theory. *Microporous Mesoporous Mater.* **2012**, *160*, 47–66. <https://doi.org/https://doi.org/10.1016/j.micromeso.2012.04.043>.
- (52) Schneider, P. Adsorption Isotherms of Microporous-Mesoporous Solids Revisited. *Appl. Catal. A Gen.* **1995**, *129*, 157–165.
- (53) Mieville, R. L. Measurement of Microporosity in the Presence of Mesopores. *J. Colloid Interface Sci.* **1972**, *41* (2), 371–373. [https://doi.org/https://doi.org/10.1016/0021-9797\(72\)90123-3](https://doi.org/https://doi.org/10.1016/0021-9797(72)90123-3).
- (54) Lippens, B. C.; de Boer, J. H. Studies on Pore Systems in Catalysts: V. The t Method. *J. Catal.* **1965**, *4* (3), 319–323. [https://doi.org/10.1016/0021-9517\(65\)90307-6](https://doi.org/10.1016/0021-9517(65)90307-6).
- (55) Neimark, A. V. Fractal Analysis. In *Handbook of Porous Solids*; Schüth, F., Sing, K. S. W., Weitkamp, J., Eds.; Wiley-VCH Verlag GmbH & Co.: Weinheim, 2002; p 3208. <https://doi.org/10.1002/9783527618286>.
- (56) Pfeifer, P.; Wu, Y. J.; Cole, M. W.; Krim, J. Multilayer Adsorption on a Fractally Rough Surface. *Phys. Rev. Lett.* **1989**, *62* (17), 1997–2000. <https://doi.org/10.1103/PhysRevLett.62.1997>.
- (57) Pfeifer, P.; Obert, M.; Cole, M. W. Fractal BET and FHH Theories of Adsorption: A Comparative Study. *Proc. R. Soc. Lond. A. Math. Phys. Sci.* **1989**, *423* (1864), 169–188.
- (58) Neimark, A. V. Thermodynamic Method for Calculating Surface Fractal Dimension. *JETP Lett.* **1990**, *51* (10), 607.
- (59) Wang, F.; Li, S. Determination of the Surface Fractal Dimension for Porous Media by Capillary Condensation. *Ind. Eng. Chem. Res.* **1997**, *36* (5), 1598–1602. <https://doi.org/10.1021/ie960555w>.
- (60) Sandoval-Díaz, L.-E.; Aragon-Quiroz, J.-A.; Ruíz-Cardona, Y.-S.; Domínguez-Monterroza, A.-R.; Trujillo, C.-A. Fractal Analysis at Mesopore Scale of Modified USY Zeolites by Nitrogen Adsorption: A Classical Thermodynamic Approach. *Microporous Mesoporous Mater.* **2017**, *237*, 260–267. <https://doi.org/https://doi.org/10.1016/j.micromeso.2016.08.030>.
- (61) Niño Celis, V. Modelamiento Fractal de La Estructura Porosa de Materiales Nanoporosos, Universidad Industrial de Santander, Bucaramanga, 2018.
- (62) Ardila-Suárez, C.; Rodríguez-Pereira, J.; Baldovino-Medrano, V. G.; Ramírez-Caballero, G. E. An Analysis of the Effect of Zirconium Precursors of MOF-808 on Its Thermal Stability, and Structural and Surface Properties. *CrystEngComm* **2019**, *21* (9), 1407–1415. <https://doi.org/10.1039/c8ce01722k>.
- (63) Ardila-Suárez, C.; Díaz-Lasprilla, A. M.; Díaz-Vaca, L. A.; Balbuena, P. B.; Baldovino-Medrano, V. G.; Ramírez-Caballero, G. E. Synthesis, Characterization, and Post-Synthetic Modification of a Micro/Mesoporous Zirconium-Tricarboxylate

- Metal-Organic Framework: Towards the Addition of Acid Active Sites. *CrystEngComm* **2019**, *21*, 3014–3030. <https://doi.org/10.1039/c9ce00218a>.
- (64) Fernández, F.; Berríos, C.; Garrido-Ramírez, E.; Escalona, N.; Gutiérrez, C.; Ureta-Zañartu, M. S. Electrooxidation of 2-Chlorophenol and 2,4,6-Chlorophenol on Glassy Carbon Electrodes Modified with Graphite–Zeolite Mixtures. *J. Appl. Electrochem.* **2014**, *44* (12), 1295–1306. <https://doi.org/10.1007/s10800-014-0763-2>.
- (65) Schmidt, F.; Hoffmann, C.; Giordanino, F.; Bordiga, S.; Simon, P.; Carrillo-Cabrera, W.; Kaskel, S. Coke Location in Microporous and Hierarchical ZSM-5 and the Impact on the MTH Reaction. *J. Catal.* **2013**, *307*, 238–245. <https://doi.org/https://doi.org/10.1016/j.jcat.2013.07.020>.
- (66) Thommes, M. Physical Adsorption Characterization of Nanoporous Materials. *Chemie Ing. Tech.* **2010**, *82* (7), 1059–1073. <https://doi.org/https://doi.org/10.1002/cite.201000064>.
- (67) Lippens, B. C.; Boer, J. H. d. Studies on Pore Systems in Catalysts III. Pore-Size Distribution Curves in Aluminum Oxide Systems. *J. Catal.* **1964**, *3* (1), 44–49. [https://doi.org/https://doi.org/10.1016/0021-9517\(64\)90091-0](https://doi.org/https://doi.org/10.1016/0021-9517(64)90091-0).
- (68) Duarte, L.; Garzón, L.; Baldovino-Medrano, V. G. An Analysis of the Physicochemical Properties of Spent Catalysts from an Industrial Hydrotreating Unit. *Catal. Today* **2019**, *338*. <https://doi.org/10.1016/j.cattod.2019.05.025>.
- (69) Baldovino-Medrano, V. G.; Farin, B.; Gaigneaux, E. M. Effect of Secondary Additives on the Properties of Vanadium-aluminum Mixed Oxide Tableted Catalysts Used in the Oxidation of Propane. *Powder Technol.* **2021**, *387*, 181–196. <https://doi.org/https://doi.org/10.1016/j.powtec.2021.03.067>.
- (70) Sing, K. S. W.; Everett, D. H.; Haul, R. A. W.; Moscou, L.; Pierotti, R. S.; Rouquerol, J.; Siemieniewska, T. Reporting Physisorption Data for Gas/Solid Systems with Special Reference to the Determination of Surface Area and Porosity. *Pure Appl. Chem.* **1985**, *57* (4), 603–619. <https://doi.org/10.1351/pac198557040603>.
- (71) Bird, R. B.; Stewart, W. E.; Lightfoot, E. N. *Transport Phenomena*, 1st ed.; John Wiley & Sons: New York, NY, 1960.
- (72) Anderson, S. L.; Lubner, E. J.; Olsen, B. C.; Buriak, J. M. Substance over Subjectivity: Moving beyond the Histogram. *Chem. Mater.* **2016**, *28* (17), 5973–5975. <https://doi.org/10.1021/acs.chemmater.6b03430>.
- (73) Kärger, J. Transport Phenomena in Nanoporous Materials. *ChemPhysChem* **2015**, *16* (1), 24–51. <https://doi.org/https://doi.org/10.1002/cphc.201402340>.
- (74) Lai, W.; Yang, S.; Jiang, Y.; Zhao, F.; Li, Z.; Zaman, B.; Fayaz, M.; Li, X.; Chen, Y. Artefact Peaks of Pore Size Distributions Caused by Unclosed Sorption Isotherm and Tensile Strength Effect. *Adsorption* **2020**, *26* (4), 633–644. <https://doi.org/10.1007/s10450-020-00228-1>.

Supplementary Information

Systematic analysis of the nitrogen adsorption-desorption isotherms recorded for a series of microporous – mesoporous amorphous aluminosilicates using classical methods

Víctor G. Baldovino-Medrano^{a,c,d,e,*},  Viviana Niño-Celis^{b,d}, Rafael Isaacs-Giraldo^{b,*}

^aEscuela de Ingeniería Química, Universidad Industrial de Santander, Clle 9 Cra 27, Ciudad Universitaria, Bucaramanga, (Santander) 680002

^bEscuela de Matemáticas, Universidad Industrial de Santander, Clle 9 Cra 27, Ciudad Universitaria, Bucaramanga, (Santander) 680002

^cCentro de Materiales y Nanociencias (CMN), Parque Tecnológico Guatiguará, Km. 2 vía El Refugio, Universidad Industrial de Santander, Piedecuesta (Santander), 681011, Colombia

^dCentro de Investigaciones en Catálisis (@CICATUIS), Parque Tecnológico Guatiguará, Km. 2 vía El Refugio, Universidad Industrial de Santander, Piedecuesta (Santander), 681011, Colombia

^eLaboratorio de Ciencia de Superficies (@CSSS UIS), Parque Tecnológico Guatiguará, Km. 2 vía El Refugio, Universidad Industrial de Santander, Piedecuesta (Santander), 681011, Colombia

*Corresponding authors. E-mail: vicbaldo@uis.edu.co; rafaisaacs@saber.uis.edu.co

List of Figures and Tables

Figure S1. N ₂ physisorption isotherms (77K) for the studied materials.....	40
Figure S2. C _{BET} constant ¹ plotted as a function of the micropore surface area (Micro-SA) - estimated by the t-plot method using the Harkins and Jura model isotherm ² - of the studied materials.	44
Figure S3. Typical linear fittings for estimating the fractal dimension of ASA050 according to the methods by Pfeifer et al. ^{3,4} , Neimark, ^{5,6} Wang and Li, ⁷ and Sandoval et al. ⁸	45
Figure S4. Fractal dimension as a function of the surface area of the materials.	46
Figure S5. Fractal dimension as a function of the percentage of the micropore surface area (ξ) of the materials.....	46
Table 1. Fractal dimensions as estimated with the methods by Pfeifer et al. ^{3,4} , Neimark, ^{5,6} Wang and Li, ⁷ and Sandoval et al. ⁸	47

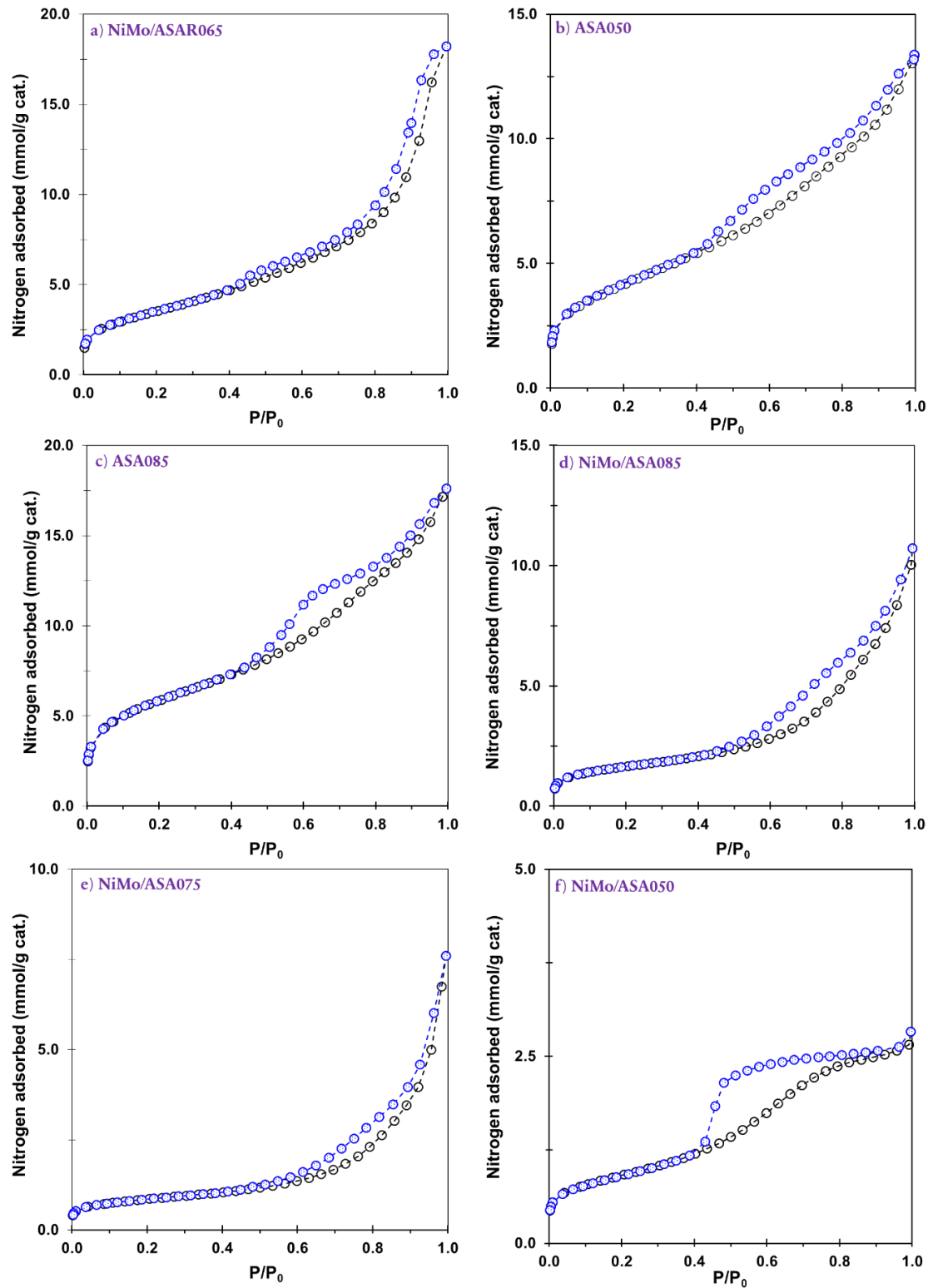


Figure S1. N₂ physisorption isotherms (77K) for the studied materials.

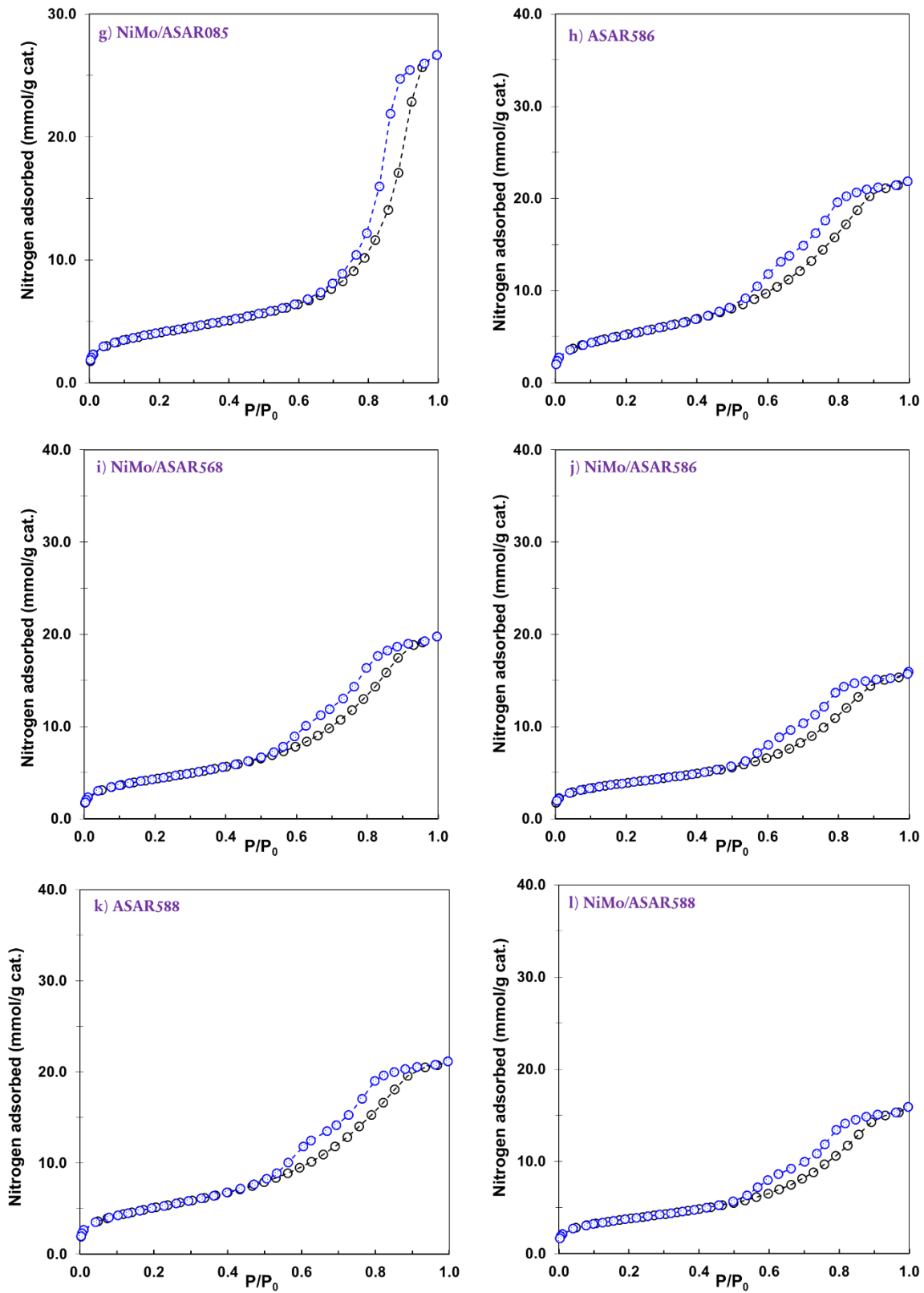


Figure S1 (continuation). N_2 physisorption isotherms (77K) for the studied materials.

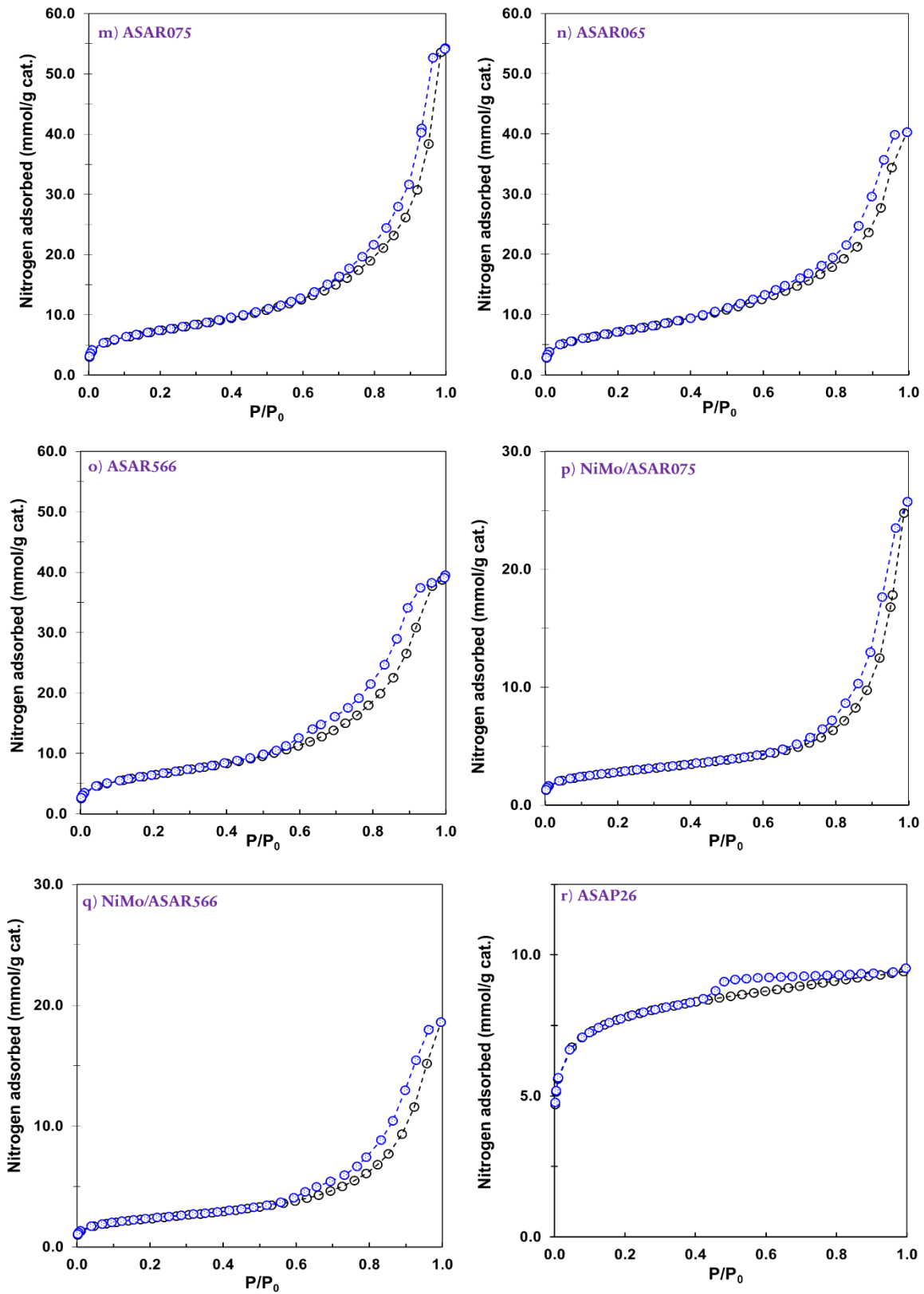


Figure S1 (continuation). N_2 physisorption isotherms (77K) for the studied materials.

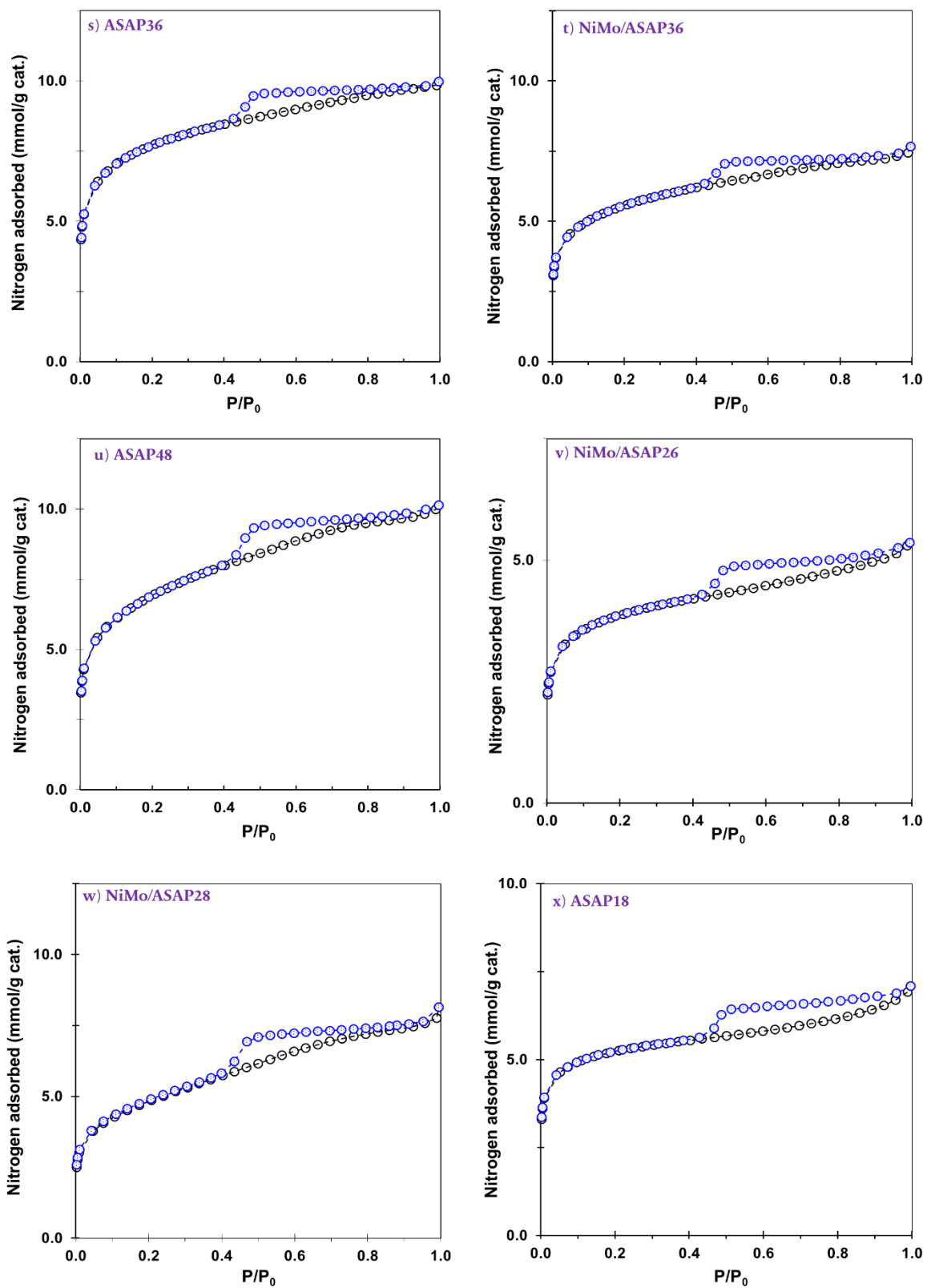


Figure S1 (continuation). N₂ physisorption isotherms (77K) for the studied materials.

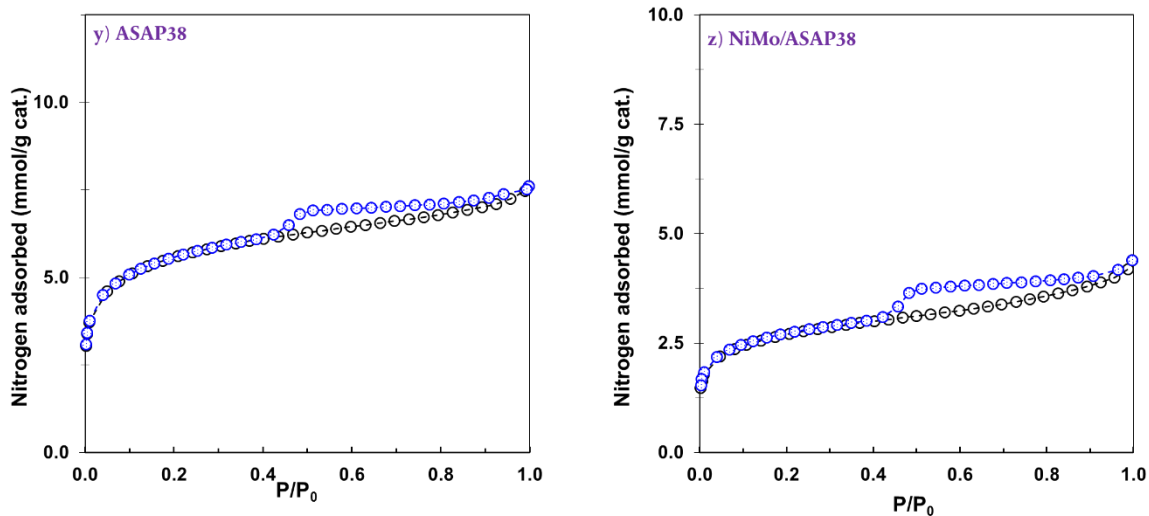


Figure S1 (continuation). N_2 physisorption isotherms (77K) for the studied materials.

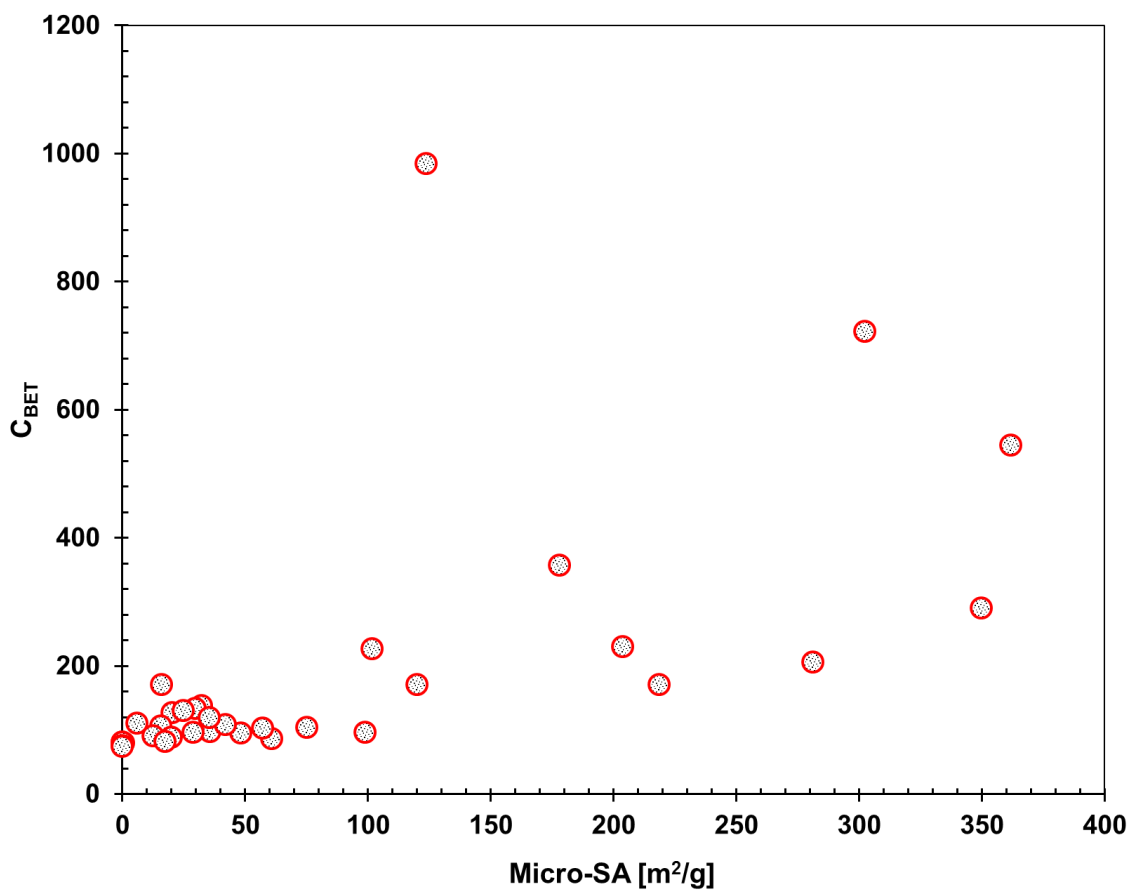


Figure S2. C_{BET} constant¹ plotted as a function of the micropore surface area (Micro-SA) -estimated by the t-plot method using the Harkins and Jura model isotherm²- of the studied materials.

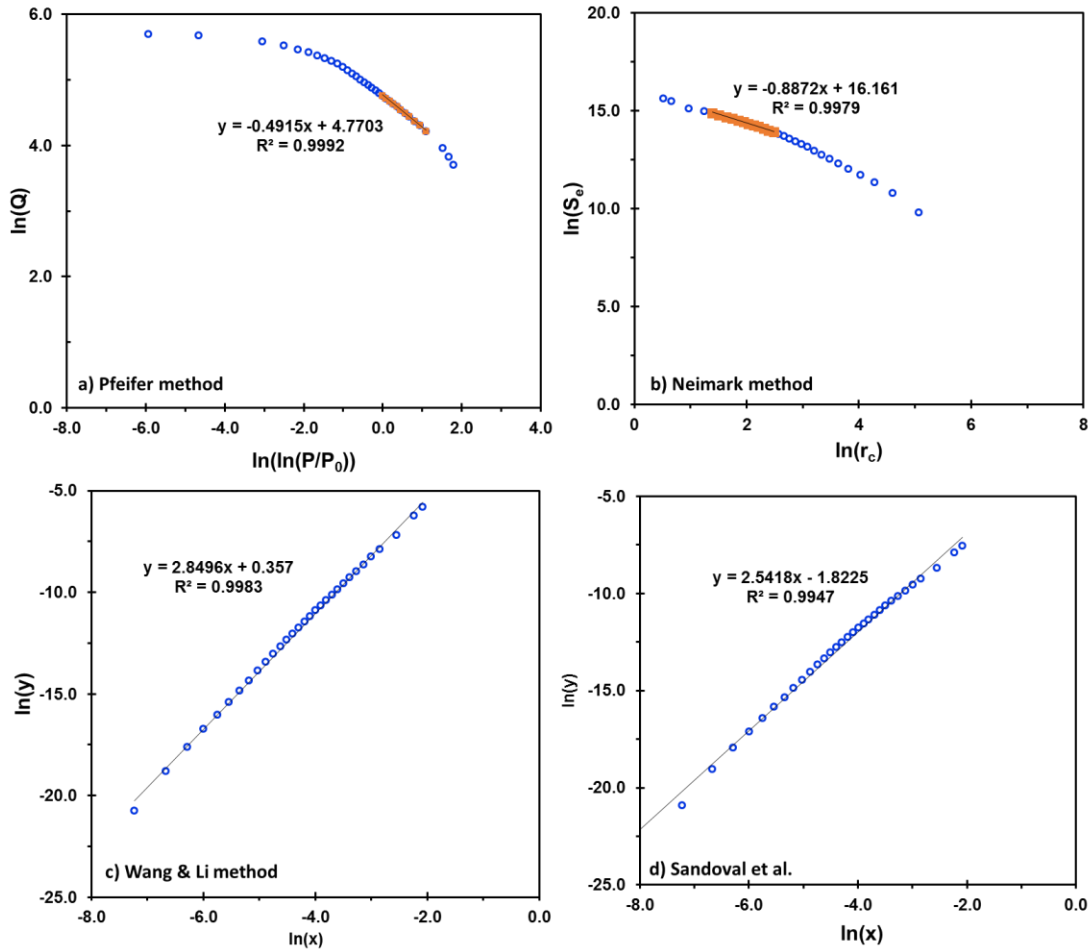


Figure S3. Typical linear fittings for estimating the fractal dimension of ASA050 according to the methods by Pfeifer et al.^{3,4}, Neimark,^{5,6} Wang and Li,⁷ and Sandoval et al.⁸

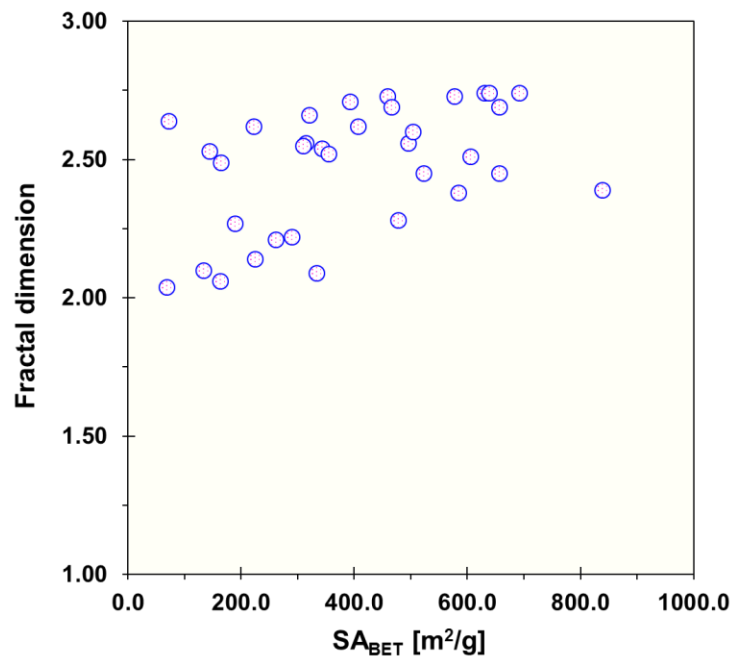


Figure S4. Fractal dimension as a function of the surface area of the materials.

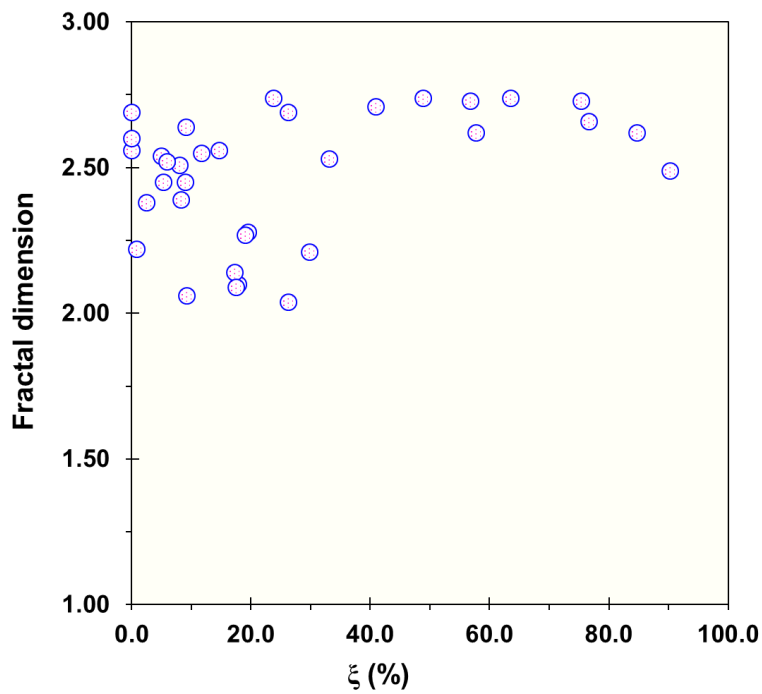


Figure S5. Fractal dimension as a function of the percentage of the micropore surface area (ξ) of the materials.

Table S1. Fractal dimensions as estimated with the methods by Pfeifer et al.^{3,4}, Neimark,^{5,6} Wang and Li,⁷ and Sandoval et al.⁸

Material code	Pfeifer	Neimark	Wang & Li	Sandoval et al.
ASA05	2.50	2.88	2.84	2.54
NiMo/ASA05	2.55	2.74	2.92	2.64
ASA075	2.56	2.56	2.55	2.21
NiMo/ASA075	2.57	2.46	2.48	2.04
ASA085	2.61	2.65	2.61	2.28
NiMo/ASA085	2.63	2.42	2.44	2.10
ASA095	2.86	2.97	2.72	2.39
NiMo/ASA085	2.85	2.27	2.40	2.06
ASAP18	2.85	3.28	2.92	2.62
NiMo/ASAP18	2.89	3.15	2.82	2.49
ASAP26	2.82	3.67	3.01	2.73
NiMo/ASAP26	2.79	3.42	2.96	2.66
ASAP28	2.68	3.52	3.01	2.74
NiMo/ASAP28	2.66	3.38	2.99	2.71
ASAP36	2.77	3.63	3.01	2.74
NiMo/ASAP36	2.74	3.64	3.01	2.73
ASAP38	2.77	3.63	2.98	2.69
NiMo/ASAP38	2.75	3.30	2.92	2.62
ASAP48	2.67	3.55	3.01	2.74
NiMo/ASAP48	2.63	2.96	2.84	2.53
ASAR065	2.51	2.64	2.71	2.38
NiMo/ASAR065	2.55	2.50	2.55	2.22
ASAR075	2.51	2.59	2.81	2.51
NiMo/ASAR075	2.57	2.46	2.48	2.14
ASAR085	2.54	2.52	2.77	2.45
NiMo/ASAR085	2.63	2.42	2.44	2.09
ASAR566	2.52	2.52	2.77	2.45
NiMo/ASAR566	2.58	2.45	2.60	2.27
ASAR568	2.48	2.60	2.84	2.56
NiMo/ASAR568	2.52	2.56	2.81	2.52
ASAR586	2.50	2.60	2.88	2.60
NiMo/ASAR586	2.57	2.56	2.85	2.56
ASAR588	2.49	3.00	2.88	2.69
NiMo/ASAR588	2.55	2.57	2.84	2.55

References

- (1) Brunauer, S.; Emmett, P. H.; Teller, E. Adsorption of Gases in Multimolecular Layers. *J. Am. Chem. Soc.* **1938**, *60* (2), 309–319. <https://doi.org/10.1021/ja01269a023>.
- (2) Lippens, B. C.; de Boer, J. H. Studies on Pore Systems in Catalysts: V. The t Method. *J. Catal.* **1965**, *4* (3), 319–323. [https://doi.org/10.1016/0021-9517\(65\)90307-6](https://doi.org/10.1016/0021-9517(65)90307-6).
- (3) Pfeifer, P.; Wu, Y. J.; Cole, M. W.; Krim, J. Multilayer Adsorption on a Fractally Rough Surface. *Phys. Rev. Lett.* **1989**, *62* (17), 1997–2000. <https://doi.org/10.1103/PhysRevLett.62.1997>.
- (4) Pfeifer, P.; Obert, M.; Cole, M. W. Fractal BET and FHH Theories of Adsorption: A Comparative Study. *Proc. R. Soc. Lond. A. Math. Phys. Sci.* **1989**, *423* (1864), 169–188.
- (5) Neimark, A. V. Fractal Analysis. In *Handbook of Porous Solids*; Schüth, F., Sing, K. S. W., Weitkamp, J., Eds.; Wiley-VCH Verlag GmbH & Co.: Weinheim, 2002; p 3208. <https://doi.org/10.1002/9783527618286>.
- (6) Neimark, A. V. Thermodynamic Method for Calculating Surface Fractal Dimension. *JETP Lett.* **1990**, *51* (10), 607.
- (7) Wang, F.; Li, S. Determination of the Surface Fractal Dimension for Porous Media by Capillary Condensation. *Ind. Eng. Chem. Res.* **1997**, *36* (5), 1598–1602. <https://doi.org/10.1021/ie960555w>.
- (8) Sandoval-Díaz, L.-E.; Aragon-Quiroz, J.-A.; Ruíz-Cardona, Y.-S.; Domínguez-Monterroza, A.-R.; Trujillo, C.-A. Fractal Analysis at Mesopore Scale of Modified USY Zeolites by Nitrogen Adsorption: A Classical Thermodynamic Approach. *Microporous Mesoporous Mater.* **2017**, *237*, 260–267. <https://doi.org/https://doi.org/10.1016/j.micromeso.2016.08.030>.
- (9) Horváth, G.; Kawazoe, K. Method for the Calculation of Effective Pore Size Distribution in Molecular Sieve Carbon. *J. Chem. Eng. Japan* **1983**, *16* (6), 470–475. <https://doi.org/10.1252/jcej.16.470>.
- (10) Saito, A.; Foley, H. C. Curvature and Parametric Sensitivity in Models for Adsorption in Micropores. *AIChE J.* **1991**, *37* (3), 429–436. <https://doi.org/https://doi.org/10.1002/aic.690370312>.
- (11) Barrett, E. P.; Joyner, L. G.; Halenda, P. P. The Determination of Pore Volume and Area Distributions in Porous Substances. I. Computations from Nitrogen Isotherms. *J. Am. Chem. Soc.* **1951**, *73* (1), 373–380. <https://doi.org/10.1021/ja01145a126>.
- (12) Harkins, W. D.; Jura, G. An Adsorption Method for the Determination of the Area of a Solid without the Assumption of a Molecular Area, and the Area Occupied by Nitrogen Molecules on the Surfaces of Solids. *J. Chem. Phys.* **1943**, *11* (9), 431–432. <https://doi.org/10.1063/1.1723871>.